RICE UNIVERSITY

Viscoelasticity of Single-Walled Carbon Nanotube Solutions with Tunable Attractive Interactions

by

Colin Christopher Young

A Thesis Submitted
in Partial Fulfillment of the
Requirements for the Degree

Master of Science

Approved, Thesis Committee:

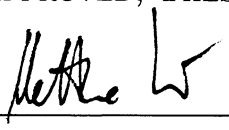

Matteo Pasquali
Professor in Chemical and Biomolecular Engineering

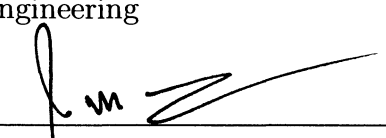

Pulickel M. Ajayan
Benjamin M. and Mary Greenwood Anderson Professor in Engineering
Materials Science and Nanotechnology

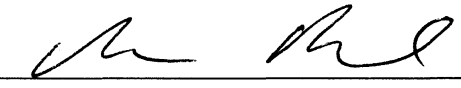

Sibani L. Biswal
Assistant Professor in Chemical and Biomolecular Engineering

Douglas Natelson
Professor in Physics and Astronomy

Houston, Texas

August, 2011

Viscoelasticity of Single-Walled Carbon Nanotube Solutions with Tunable Attractive Interactions

by

Colin Christopher Young

Abstract

Understanding the microstructure of single walled nanotubes (SWNTs) in solution is an essential step in the development of fluid processing techniques for the creation of multifunctional macroscopic SWNT materials and is also useful in the more fundamental study of rigid rod solutions. In this thesis, the microstructure of SWNT solutions in $ClHSO_3$ and in mixtures of $ClHSO_3$ and 102% H_2SO_4 is studied by investigation of their viscoelastic properties. These results are compared to previous investigations of SWNTs in 102% H_2SO_4 and in $ClHSO_3$ at higher concentrations in order to study the effects of concentration and inter-SWNT attractive potential. Attractive interactions between the SWNTs are found to have a strong effect on percolation threshold concentration. A percolation transition is also observed in solutions at a fixed concentration as the solvent strength is decreased. Measurements obtained below the percolation transition are compared to the predictions of existing rigid rod solution models.

Table of Contents

Abstract i

Table of Contents ii

List of Figures iv

1 Introduction 1

2 Background 7

2.1 Carbon Nanotubes 7

2.1.1 Structure and Properties 8

2.1.2 Synthesis 9

2.2 Carbon Nanotube Solutions 12

2.2.1 CNT/Superacid Solutions 12

2.2.2 Phase Behavior 13

2.3 Rigid Rod Solutions 15

2.3.1 Liquid Crystals 17

2.3.2 Viscoelasticity in Isotropic Solutions 17

2.3.3 Rigid Rod Percolation 23

3 Materials and Methods 26

3.1 Preparation of Solutions 27

3.2 Microscopy 28

3.3 Rheology 28

3.3.1 Experimental Setup 28
3.3.2 Dynamic shear tests 32
3.3.3 Experimental Limitations 34

4 Effect of Solvent Strength and Concentration on Microstructure **39**
4.1 Varying Concentration 39
4.1.1 Phases of SWNT solutions 40
4.1.2 Experimental Results 42
4.1.3 Percolation 52
4.1.4 Comparison to Theory 59
4.1.4.1 Suitability of the assumption that orientational stress is dominant 60
4.1.4.2 Description of the model 63
4.1.4.3 Comparison of the model with experimental data 66
4.2 Varying Solvent Strength 70

5 Conclusion **75**

Bibliography **80**

List of Figures

2.1 CNT Chiral Vectors 10
2.2 SWNT Molecular Models 11
2.3 Rigid Rod Concentration Regimes 16
2.4 Types of Liquid Crystal 18
2.5 Reptation Model 19
2.6 Rigid Rod Network Contact Models 25

3.1 Rheometer Testing Geometries 29
3.2 Stainless Steel Couette and Plexiglas Cover 31
3.3 Strain Sweep Test Example 33
3.4 Frequency Sweep Test Example 34
3.5 Measurement Error Due To Rotor Inertia 37

4.1 Strain Sweep Test Results for SWNTs in $ClHSO_3$ 43
4.2 Loss Modulus of SWNT/Superacid Solutions vs. Concentration 44
4.3 Critical Strain of SWNT/Superacid Solutions vs. Concentration 45
4.4 Frequency Sweep Test Results for SWNTs in $ClHSO_3$ 47
4.5 SWNT Viscoelastic moduli at 0.1 rad/s in $ClHSO_3$ 48
4.6 SWNT Viscoelastic Moduli at 2.5 rad/s in $ClHSO_3$ 48
4.7 Comparison of Mopdulus vs. Concentration in $ClHSO_3$ and 102% H_2SO_4 49
4.8 Loss Modulus of SWNT/Superacid Solutions vs. Concentration 51
4.9 Frequency Dependence of Moduli vs. Concentration 52
4.10 Critical Percolation Behavior 54

4.11 Percolated SWNT Microstructure 55
4.12 Viscoelastic Modulus Rescaling by Concentration-dependent Factors 58
4.13 HiPco Length Distribution 60
4.14 Rigid Rod Theory Neglecting Flexibility vs. Observed Viscoelasticity in $ClHSO_3$ . . . 67
4.15 Rod Theory with Effects of Flexibility vs. Observed Viscoelasticity in $ClHSO_3$ 67
4.16 Rod Theory vs. Observed Viscoelasticity in $ClHSO_3$ Assuming Shorter Length 69
4.17 Light Microscopy of SWNTs in Superacid Mixtures 71
4.18 Polarized Light Microscopy of SWNTs in Superacid Mixtures 71
4.19 Viscoelastic Modulus and Solvent Viscosity vs. Superacid Composition 72
4.20 Loss Modulus vs. Solvent Strength 73
4.21 Critical strain vs. Solvent Strength 74

Chapter 1

Introduction

This thesis investigates the microstructure of solutions of single-walled carbon nanotubes (SWNTs) in superacids through rheological measurements, and reveals how that microsctructure depends on both the concentration of SWNTs and the attractive forces between them. This work builds upon recent research into the solvation of SWNTs in superacids and the phase behavior that has been identified for HiPco SWNTs in these solvents (Ramesh *et al.*, 2004; Davis *et al.*, 2004, 2009; Parra-Vasquez *et al.*, 2010). The processing of SWNTs, and more generally carbon nanotubes (CNTs), in a fluid phase is an area of research that holds great promise for unlocking the potential of SWNT materials in a wide range of applications. Fluid processing offers a route toward manipulating the arrangement of SWNTs within such materials on the microscopic scale, a task whose challenge has thus far hindered attempts to achieve properties near those of individual SWNTs in a macroscopic article. Understanding and controlling the microstructure of SWNT fluids is a key step toward tailoring the microstructure of solid SWNT materials.

Individual SWNTs possess outstanding thermal, electrical, and mechanical properties. On the level of a single molecule they possess a tensile strength and tensile modulus higher than those of steel, thermal conductivity better than diamond, and, in the case of SWNTS with metallic character, electrical conductivity higher than copper (Hone *et al.*, 2000; Baughman *et al.*, 2002; Yamamoto *et al.*, 2008). In addition, SWNT bundles have a density lower than graphite, and extremely high thermal stability. These properties are highly sought after in many applications,

such as the fabrication of high strength/low weight material for aerospace construction, multifunctional fibers that combine mechanical reinforcement with electrical or thermal conductivity, conductive thin films for touch screens and sensors, durable high-surface-area structures for hydrogen storage, components for field emission devices, and reinforcement in polymer composite materials. The fact that SWNTs possess these properties in combination makes them even more appealing, because they are uniquely suited for the fabriaction of multifunctional materials.

The fabrication of macroscopic SWNT materials with properties that approach those of a single SWNT has proven challenging due to the difficulty of re-arranging SWNT microsctructures from those that are adopted during their synthesis. SWNTs tend to form tight bundles held together by van der Waals forces, and these bundles are difficult to separate (Thess *et al.*, 1996). Dispersion in a fluid offers a promising route to manipulating SWNT structure; in addition, fluid processing techniques offer scalability in the manufacture of materials. However, there are very few solvents or dispersion techniques that can effectively de-bundle SWNTs or disperse them at high concentrations.

The most promising technique for achieving SWNT fluids is solvation in superacids such as chlorosulfonic acid ($ClHSO_3$) and sulfuric acid (102% H_2SO_4). With this technique, solutions of individually dispersed nanotubes can be achieved at high concentrations (Davis *et al.*, 2009). Furthermore, it has been demonstrated that exposure to superacids and subsequent acid removal does not alter the molecular structure or properties of the SWNTS, as is the case with other methods of dispersal such as debundling through sonication or dispersal through chemical functionalization. In recent years, processes have been demonstrated for the fabrication of continuous fibers and thin conducting films from SWNT/acid solutions (Ericson *et al.*, 2004; Ma *et al.*, 2011).

In any material fabricated from a fluid precursor, the microstructure of the fluid has a strong influence on the microstructure of the resulting solid article. Therefore, for any fluid processing step that has at its ultimate goal the proper arrangement of SWNTs in a material to maximize their contribution to the material properties, researchers must first investigate the structure of

SWNT solutions and how to control that structure. Four key factors are expected to influence microstructure in a SWNT solution, and theoretically all four can be controlled; these are the aspect ratio of SWNTs (the ratio of length to diameter), their flexibility (a function of diameter), the concentration of SWNTs in solution, and the strength of the attractive forces acting between the SWNTs (Solomon and Spicer, 2010).

The strength of these attractive forces can be controlled by mixing $ClHSO_3$, a solvent in which inter - CNT attraction is negligible, with H_2SO_4, in which there is a weak attraction between the CNTs. Recent work has investigated how the solubility and phase behavior of SWNTs produced by the HiPco process depend on concentration and solvent strength by using mixtures of these two acids (Davis *et al.*, 2009). CNTs at low concentrations in superacids are isotropically dispersed, with no preferred orientation; they undergo a transition to a liquid crystalline phase above a certain concentration because it becomes thermodynamically favorable for them to align with their nearest neighbors. At intermediate concentrations, isotropically dispersed CNTs are in equilibrium with the liquid crystalline phase, forming a biphasic system. In weaker acids the increased attractive potential between SWNTs causes the transition to liquid crystallinity to occur at lower concentrations.

The rheological properties of polymeric solutions and colloid dispersions are strongly determined by the structure adopted by the dispersed species, and thus can be used as a means to investigate that structure. Shear rheology can be used to measure many key properties of a material, such as viscosity, yield stress, and viscoelastic moduli. As a subset of this type of measurement, dynamic shear rheology, probes the viscoelastic properties of a sample by applying a small oscillating strain and measuring the stress generated in the material in response to that strain. This is an effective way to investigate the structure present in the fluid because that structure is not disrupted during the course of the measurement so long as the strain is sufficiently small.

In the past, studies have been conducted to measure the rheological properties of SWNT solutions, including viscoelastic properties, in both 102% H_2SO_4 and in $ClHSO_3$ (Davis *et al.*, 2004; Davis, 2006; Banzola, 2008). These two solvents serve as limiting cases of a strong and a weak

superacid solvent. In 102% H_2SO_4, SWNT rheology has been investigated over 4 decades in concentration from 30 ppm to 10% (100,000 ppm) by volume, which spans the concentration range from nearly dilute solutions to the fully liquid crytsalline regime. In $ClHSO_3$ the concentration range that had been investigated prior to this work consisted only of the higher end of this concentration range, comprising biphasic and liquid crystalline solutions between 1 vol% and 11 vol%.

One of the goals of this study was to investigate the properties of SWNT solutions in $ClHSO_3$ at lower concentrations, both for the sake of comparing low concentration properties to those that have been predicted theoretically for isotropic solutions of rigid rods and for the sake of elucidating the effect of inter-SWNT attraction by making a full comparison to the behavior that has been observed in 102% H_2SO_4. A second goal of this work was to observe the change in rheological properties that can be achieved by keeping the SWNT concentration fixed and varying the solvent strength over the range between pure $ClHSO_3$ and 102% H_2SO_4.

As this thesis will describe, dynamic shear experiments were carried out for SWNT solutions in $ClHSO_3$ at concentrations from 600 ppm to 8000 ppm; experimental limitations prevented reliable measurements at concentrations lower than this. This extends the total concentration range that has been investigated in $ClHSO_3$ approximately 1.5 decades below 1.2 vol%, which was the lowest concentration previously measured (Banzola, 2008). The results of these measurements are considered in the context of those previously obtained at higher concentrations in $ClHSO_3$ and those obtained in 102% H_2SO_4. This comparison reveals that the evolution of SWNT microstructure in each acid is broadly similar, as both systems evolve from a low concentration regime that is primarily or completely isotropic to a high concentration fully liquid crystalline phase; however, the effect of attractive interactions can be observed in the details of the percolation transition that is observed at intermediate concentrations in both acids. A physical model explaining the differences in the two percolation transitions is suggested, in which solutions in $ClHSO_3$ percolate due to the jamming of primarily isotropic SWNTs, while solutions in 102% H_2SO_4 percolate due to the formation of a network of liquid crystalline domains.

The viscoelastic properties of SWNT solutions at concentrations below this percolation thresh-

old are compared to the predictions of a theoretical model for rigid rod viscoelasticity. This model is based on a calculation of viscoelastic stress due to orientational entropy, which is predicted to be the dominant type of stress on the time scales probed by these experiments. The model used accounts for the effect of length polydispersity and slight flexibility of the SWNTs. Agreement between the experimental data and the model is poor both in the case of SWNTs in $ClHSO_3$ and in the case of SWNTs in 102% H_2SO_4. The viscoelastic properties of SWNTs in superacid solutions appear to scale more weakly with increasing SWNT concentration than the model predicts. Possible reasons for this discrepancy are briefly discussed.

Dynamic shear results were also carried out on solutions in which the volume concentration of SWNTs was held constant, but in which the strength of the solvent was varied by mixing 102% H_2SO_4 with $ClHSO_3$. In these experiments the viscous modulus of the solutions appears to change in proportion to the viscosity of the solvent itself (i.e., due to the higher viscosity of solvents containing more 102% H_2SO_4). The effect of SWNT attraction on structure is demonstrated, however, by the increase of the elastic modulus and the decrease in the loss modulus $\tan(\delta)$, which represents the ratio of viscous modulus to elastic modulus. At this concentration, SWNTs exhibit a transition from an isotropic to a percolated liquid crystalline solution as the solvent quality is decreased.

The organization of the remaining sections is as follows: Chapter 2 provides background on SWNT structure and properties and on past work that has been carried out on solutions of SWNTs in superacids. It also discusses the measurement of viscoelastic fluid properties, and some of the theoretical predictions that have been made for the phase behavior and viscoelastic properties of rigid rod solutions. Chapter 3 describes the materials and experimental methods used in this work, including light microscopy and rheological testing of SWNT/superacid solutions, as well as the sources of error that limit the experimentally accessable SWNT concentration range. Chapter 4 begins by reporting the experimental results and comparing them to the results of previous studies. It then discusses percolation in SWNT/superacid solutions and comparison of the experimental results with rigid rod solution models. Chapter 4 concludes with a discussion of dynamic shear results obtained for SWNTs in superacid solvents of varying strength. Finally,

Chapter 5 summarizes the conclusions that can be drawn from this work and the implications for future work on SWNT/superacid systems.

Chapter 2

Background

This chapter provides background information relevant to the research presented in this thesis. The topics covered here include basic information about CNTs as a class of material, the synthesis of SWNTs using the HiPco process, and the formation and phase behavior of single walled nanotube solutions in superacids. A theoretical discussion of the microstructure and viscoelastic properties of rigid rod solutions is also provided.

2.1 Carbon Nanotubes

Carbon nanotubes (CNTs) are an allotrope of carbon discovered by Iijima in 1991. They are cylindrical molecules with extremely high aspect ratio and an atomic structure similar to that of graphite, which grants them high strength and stiffness. In the years since their discovery, CNTs have been the subject of much research in the field of applied nanotechnology. Widespread interest in CNTs has been fueled by the fact that they possess a novel combination of useful properties; these properties make them an appealing material for a great many applications in the fields of electronics, materials science, and biological science. Researchers have devoted much effort to understanding the properties of individual CNTs and to solving the challenges involved in using them for various applications.

2.1.1 Structure and Properties

CNTs possess outstanding thermal, electrical, and mechanical properties. On the level of individual molecules, CNTs have been measured to have a tensile strength of at least 37 GPa (Walters *et al.*, 1999; Yu *et al.*, 2000) and Young's modulus of $\sim$ 1 TPa (Gao *et al.*, 1998; Krishnan *et al.*, 1998; Yu *et al.*, 2000), and thermal conductivity of 3000 W/mK (Hone *et al.*, 1999). In terms of electrical properties, CNTs may be either conductors, with electrical resistivity as low as 5 $\mu\Omega$cm and current carrying capacity as high as 10^9 A/cm (Ebbesen *et al.*, 1996; Wei *et al.*, 2001), or variable band gap semiconductors (Hamada *et al.*, 1992). In addition to these properties, CNTs have a low density ($1-2\,\mathrm{g/cm^3}$) and can potentially be used to make lightweight high-performance materials. It is not clear whether materials can be made out of CNTs in such a way that they retain these outstanding properties on a macroscopic scale, and further research on this question is essential to the development of CNT applications.

In terms of moleular structure, CNTs can be thought of as sheets of graphene rolled up and joined seamlessly into hollow cylinders with 1 or more concentric graphitic walls. As such, they are composed primarily of sp2-hybridized carbon atoms in a planar lattice with occasional defects such as the substitution of sp3-hybridized carbon or holes in the hexagonal carbon lattice. Single walled carbon nanotubes (SWNTs) consist of only one graphitic cylinder, which may have either open ends or ends capped with a hemisphere of sp2-carbon.

A planar graphitic lattice can be rolled seamlessly into a cylinder by matching carbon atoms at the boundary. This constraint provides a discrete set of possible chiral vectors $\mathbf{C_h}$ such that

$$\mathbf{C_h} = n\mathbf{a}_1 + m\mathbf{a}_2 \tag{2.1}$$

in which $\mathbf{a}_1$ and $\mathbf{a}_2$ are the unit vectors of the hexagonal lattice. The integer pair (n,m) determines the diameter of the SWNT according to

$$d = \frac{\mathbf{C_h}}{\pi} = \frac{\sqrt{3}a\sqrt{m^2+mn+n^2}}{\pi} \tag{2.2}$$

where $a = 0.42\,\mathrm{nm}$ is the carbon-carbon bond length. The index (m,n) also determines the

chirality of the SWNT, i.e. the angle that the unit vectors of the lattice make with the axis of the nanotube. Figure 2.1 part (a) shows how $\mathbf{C_h}$ is constructed for a (4,2) SWNT.

SWNT chiralities can be divided into three broad classes. SWNTs for which $n = m$ are denoted as "armchair" SWNTs, and SWNTs with $n = 0$ are "zigzag" SWNTs, both in reference to the pattern formed by the carbon lattice along the axis of the SWNT. All other SWNTs are called "chiral" in reference to the fact that they do not posses mirror symmetry about the SWNT axis. The chirality of a SWNT determines whether it acts as a metallic conductor or a semiconductor. Armchair SWNT and any SWNT for which $(m - n)$ is an even multiple of 3 behave as metallic conductors. A mapping of nanotube chiralities onto a graphitic lattice is provided in Figure 2.1 part (b), and Figure 2.2 depicts the molecular structures of an armchair, a zigzag, and a chiral SWNT.

2.1.2 Synthesis

The synthesis methods that have been employed to produce CNTs include arc discharge, laser ablation, chemical vapor deposition (CVD), and gas phase catalytic growth (Dai, 2001). The size and morphology of CNTs that can be produced vary greatly depending on the method and synthesis conditions used.

The HiPco (**H**igh **P**ressure **C**arbon **M**onoxide) process is a gas phase catalytic growth process, i.e., one in which SWNTs grow from catalyst particles suspended by a gas flow with a gaseous carbon source as the carbon feedstock. In the HiPco process, carbon monoxide at a pressure of 10-30 atm is used as both the carbon source and the carrier gas for the catalyst particles. The catalyst particles used are iron generated by the decomposition of $Fe(CO)_5$ at temperatures of $800 - 1200\,°C$. In addition to SWNTs, material collected from the HiPco reactor typically contains fullerenes and catalyst particles coated in amorphous carbon; a multi-step purification process has been developed for the removal of this excess material. The SWNTs produced using this method are polydisperse in diameter, ranging from $0.7 - 1.4$ nm, and in length, ranging from $0.05 - 10\,\mu m$, with the majority of SWNTs having a length of less than $1\,\mu m$. Length mea-

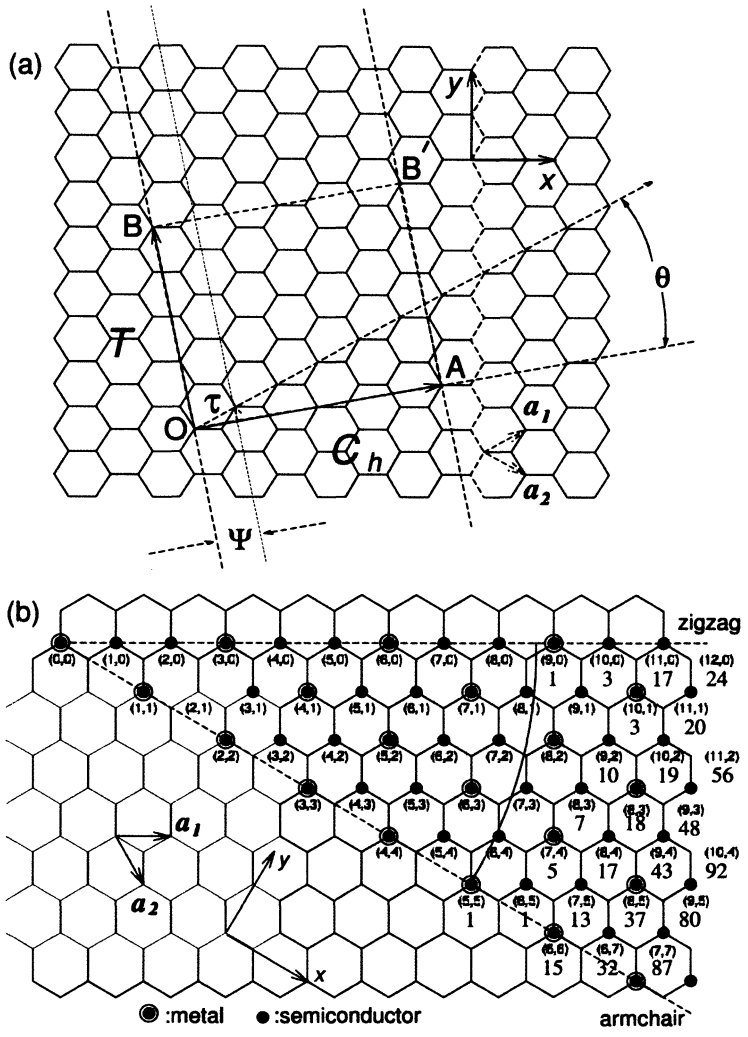

Figure 2.1: (a) Relationship of the chiral vector $\mathbf{C_h}$, the unit vectors $\mathbf{a}_1$ and $\mathbf{a}_2$, and the chiral angle θ for a (4,2) nanotube. The vector $\mathbf{OB} = \mathbf{T}$ is the lattice vector of the 1D nanotube unit cell, and is parallel to the axis of the nanotube. (b) Schematic displaying several possible chiral vectors for SWNTs, including zigzag, armchair, and chiral nanotubes. Encircled dots represent metallic nanotubes, and single dots represent semiconducting nanotubes. The ordered pair (n, m) is given for each chirality; the number given below each (n, m) designation is the number of possible end caps that can be joined to a SWNT of that chirality. Reproduced from Dresselhaus and Avouris (2001) without permission.

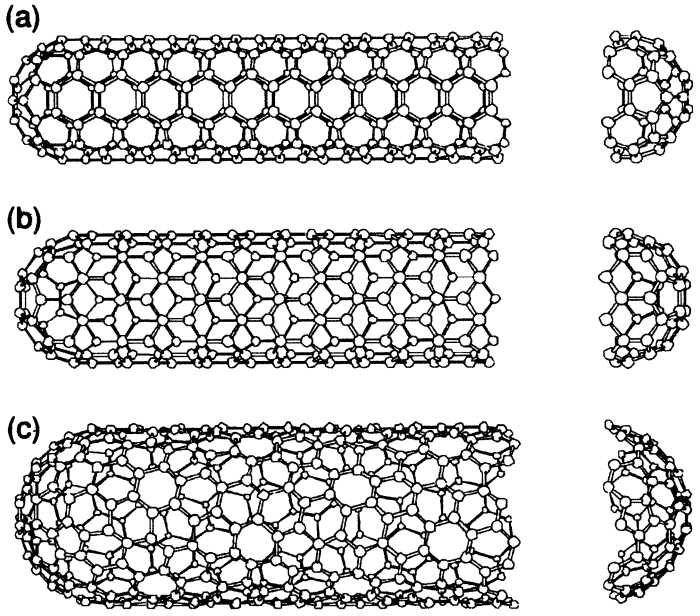

Figure 2.2: Models of (a) a (5,5) "armchair" SWNT with $\theta = 30°$, (b) a (9,0) "zigzag" SWNT with $\theta = 0°$, and (c) a (10,5) "chiral" SWNT with θ between 0° and 30°. Also shown are possible sp2-carbon end caps for these SWNTs. Reproduced from Dresselhaus and Avouris (2001) without permission.

surements performed on HiPco SWNTs using AFM indicate a lognormal length distribution with average length $\langle L \rangle$ between 0.3μm and 1.26μm (Carver *et al.*, 2005).

2.2 Carbon Nanotube Solutions

One of the obstacles to generating new technology based on CNTs is the challenge of creating **macroscopic articles that retain a significant portion of the properties of a single CNT molecule. This challenge arises from the difficulty of arranging CNTs into desired structures that will maximize** performance (transfer of mechanical stress, thermal conduction, etc). CNTs tend to form **tightly bound bundles due to van der Waals attraction, which makes it difficult to manipulate** their structure after synthesis.

One potential route towards controlling the microscopic structure of CNT materials is the **use of fluid processing. If CNTs can be separated from each other in a fluid matrix, their structure can potentially be manipulated by control of the phase behavior and flow history of the** solution. Unfortunately, the ability of conventional solvents to disperse SWNTs is limited due to the strong van der Waals bundling forces that exist between them. These forces are especially strong for closely packed and parallel CNTs because of their large surface of contact. Methods that have been employed to disperse CNTs include sonication-induced debundling followed by stabilization by polymer or surfactant wrapping (Vigolo *et al.*, 2000), functionalization to **increase solvent affinity and prevent close packing** (Hudson *et al.*, 2004; Penicaud *et al.*, 2005), and solvation at low concentrations in NMP (Bergin *et al.*, 2008). These methods fail to achive high concentrations and often result in dispersions containing CNTs that have not been completely de-bundled; furthermore, sonication and functionalization compromise the length and the properties of CNTs, and as such are not suitable processing methods for applications which seek to preserve those properties.

2.2.1 CNT/Superacid Solutions

True solutions of individually dispersed CNTs can be achieved by using superacid solvents. The term superacid denotes any acid stronger than 100% H_2SO_4. **Sufficiently strong acids have the**

ability to contribute protons to CNTs (a mechanism known as protonation) via a reaction of the form

$$C_x + yAH \rightarrow \left[C_x^{\delta+} H_y^{(1-k\delta)+}\right] + yA^- \tag{2.3}$$

This results in a net positive charge on the CNT sidewall (Ramesh *et al.*, 2004). The resulting electrostatic repulsion between positively charged CNTs can partially or completely counteract van der Waals attraction, resulting in a solution of CNTs that are only weakly attracting or even completely non-interacting (Green *et al.*, 2009).

The degree of protonation that can be achieved is related to the diameter of the CNT, the density of defects containing sp3 carbon (which is not protonated due to the lack of unbound electrons), and the strength of acid used. 102% H_2SO_4 was found to be a good solvent for SWNTs with small diameters and relatively short lengths (specifically, HiPco SWNTs), but is unable to protonate larger diameter CNTs (Duque *et al.*, 2010). In contrast, $ClHSO_3$ has been found to protonate and disperse both SWNTs and multi-walled nanotubes (MWNTs) of any length and diameter, provided that the density of sp3 carbon defects is low (Parra-Vasquez *et al.*, 2010).

2.2.2 Phase Behavior

Because $ClHSO_3$ and H_2SO_4 are miscible, they can be combined to create superacids of intermediate protonating strength. This has enabled an investigation of the phase behavior of HiPco SWNTs in superacids as a function of solvent protonation strength and SWNT concentration (Davis *et al.*, 2009).

Low concentration SWNT solutions are composed of dilute, noninteracting SWNTs with an isotropic orientation distribution. At higher concentrations the system is more crowded, and it becomes entropically favorable for SWNTs to align with their nearest neighbors to form ordered liquid crystalline domains, the presence of which has been detected by polarized light microscopy (Davis *et al.*, 2004). Above a certain concentration SWNT solutions are biphasic, containing both isotropically dispersed SWNTs and liquid crystalline domains. At even higher SWNT concentrations, the proportion of SWNTs in the liquid crystalline phase is greater; at a

sufficiently high concentration the isotropic phase vanishes. SWNT solutions above this concentration form a polydomain, fully liquid crystalline phase in which the domains themselves may be either isotropically dispersed or aligned with a director, depending on the shear history of the sample.

The theory developed by Flory to describe the liquid crystalline phase behavior of anisotropically shaped particles in solvents of varying strength predicts that using a solvent with a different strength should change the width of the biphasic concentration regime; this has been found to hold true for SWNT/superacid solutions (Flory, 1956). The biphasic regime is broader in weaker acids, with the onset concentration ϕ_{iso} occurring at much lower concentrations. The concentration ϕ_{iso} at which the biphasic regime first appears in superacids has been determined through the use of centrifugation- induced phase separation coupled with a UV-Vis-NIR light absorption technique to evaluate the concentration of the isotropic phase (Parra-Vasquez *et al.*, 2010). Centrifugation of biphasic liquid crystalline solutions results in a concentrated liquid crystalline phase in the bottom of the vial, with a supernatant of isotropic SWNTs. The concentration of this supernatant phase is equal to the concentration of isotropic SWNTs in the parent solution. A determination of this supernatant concentration using light absorptionl, coupled with knowledge of the length distribution in the system, allows for the determination of the isotropic cloud point, i.e., the lowest concentration at which liquid crystalline domains can appear. The isotropic cloud point ϕ_{iso} has been estimated to be about 3000 ppm in $ClHSO_3$; in 102% H_2SO_4 the cloud point has not been fully determined, but it is apparently well below 100 ppm, based on the results of phase separation experiments (Davis *et al.*, 2009; Green *et al.*, 2009).

In the case of SWNT solutions in 102% H_2SO_4 the transition concentration ϕ_{nem}, at which the system becomes completely liquid crystalline, has been determined through Differential Scanning Calorimetry (DSC) to be around 9 vol% (Davis *et al.*, 2009). For SWNTs in $ClHSO_3$, DSC has not yet been attempted on an instrument capable of reaching the low temperatures required to freeze the solution (solutions were found to remain liquid below -100 °C); however, application of Onsager theory for rigid rod molecules indicates that in this acid ϕ_{nem} should be around 12 vol% in $ClHSO_3$ (Green *et al.*, 2009).

The isotropic cloud point in the case of SWNTs in $ClHSO_3$ is in good agreement with the predictions of Onsager theory for rigid rods in an athermal solvent, that is, one in which the dissolved rods do not experience any attractive interaction (Green *et al.*, 2009). In this acid the electrostatic repulsion induced by protonation is enough to completely counteract the force of van der Waals attraction. This is the reason for the impressive power $ClHSO_3$ has to dissolve CNTs, in contrast with H_2SO_4, in which the theory indicates there is an attractive potential of $-2.75\,k_BT/\mu m$ between aligned HiPco SWNTs. The difference between the two acids is magnified in the case of long CNTs, because the total attractive force between CNTs with any attractive potential will scale with the length of their contact. As an athermal solvent, $ClHSO_3$ is able to dissolve CNTs up to hunderds of micrometers in length (Parra-Vasquez *et al.*, 2010). For this reason it has the potential to be an essential tool in any application requiring the use of very long CNTs such as the formation of fiber or any similar application in which SWNT interfactial friction is required as a source mechanical reinforcement.

2.3 Rigid Rod Solutions

In the context of solutions, a rigid rod is a particle or molecule with length much less than its own persistence length, $L \ll L_p$. In solution a rigid rod polymer will maintain a rod-like shape, rather than adopting a random coil structure as would a flexible polymer. Solutions containing rod-like particles are found in many biological systems, and used in a wide variety of material applications. The inclusion of rigid rods of high aspect ratio in a fluid can have a dramatic effect on its rheological properties even when the volume concentration of rods is quite low; this makes the addition of rod-like particles a very efficient way to tailor the properties of those solutions to suit a particular application. The effect of rigid rods on the viscoelasticity of solutions has been theoretically modeled by Kirkwood & Plock, Doi & Edwards, and others (Doi and Edwards, 1986; Kirkwood and Plock, 1956).

Solutions of rigid rods in a good solvent (i.e. without attractive interaction) exhibit several concentration regimes, as illustrated in Figure 2.3. In the dilute regime at low concentrations the

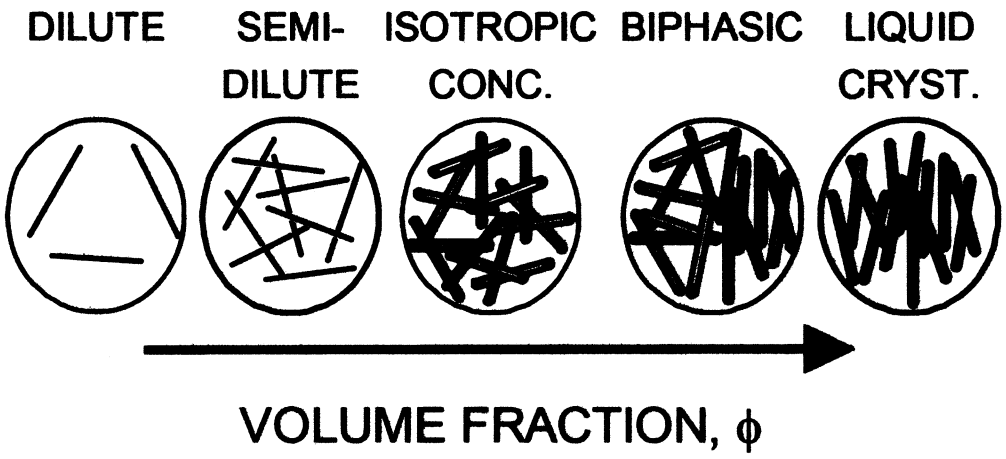

Figure 2.3: Schematic illustrating the concentration regimes that can be found in rigid rod solutions. From left to right these are: dilute, semidilute, concentrated isotropic, biphasic, and fully liquid crystalline. In an athermal solvent, the transition to liquid crystalline behavior is driven by excluded volume interactions (Reproduced from Davis *et al.* (2004) without permission, adapted from Doi and Edwards (1986)).

rods are far apart from their nearest neighbors and do not interact. At number concentrations above

$$\nu \simeq \frac{1}{L^3} \tag{2.4}$$

the rods enter the semidilute regime, in which they become close enough to hinder each other's rotational motion. At higher concentrations the rods enter a concentrated isotropic, or tightly entangled, regime, in which both rotational and translational movements are strongly hindered by the proximity of nearby rods. As the concentration increases further, it becomes entropically favorable for the rods to align with their nearest neighbors, thereby minimizing excluded volume interactions and maximizing the degree of freedom available for translational motion. At moderate concentrations, some of the rods will align into a liquid crystalline phase while others remain isotropically dispersed. At higher concentrations, the rods form a fully liquid crystalline solution (Doi and Edwards, 1986).

2.3.1 Liquid Crystals

Liquid crystalline solutions are those in which the dissolved phase exhibits spontaneous ordering. A wide variety of materials exhibit liquid crystalline behavior, including stiff polymers such as PPTA. Liquid crystals are employed in a variety of applications, such as optical displays, filters, and fibers composed of highly aligned polymer chains (Gabriel and Davidson, 2003).

Liquid crystals can be divided into two broad categories: lyotropic liquid crystals, which are composed of a rigid species of molecule or particle dispersed in a solvent, with the ordering transition being driven by excluded volume interactions, and thermotropic liquid crystals, in which liquid crystallinity is induced in a temperature range between the temperatures at which the system is a solid or a fully isotropic liquid. Liquid crystals can also be subdivided into 3 categories based on the type of ordering present. Nematic liquid crystals possess long range orientational order such that the orientation of particles within a given domain is arranged along a common director, but possess only short range positional order, which determines spacing with their nearest neighbors. Cholesteric liquid crystals are similar to nematics, but have a domain director which rotates about an axis perpendicular to that director, resulting in a twisted domain structure. Smectic liquid crystals possess long range order about a directior, but also posses long range positional order which gives them a layered structure. Typically, the particles within a given layer share a common director **n**; two common types of smectic liquid crystals are smectic type A, in which orientational ordering does not extend to other layers, and smectic type C, in which all the layers share a common director. An illustration of the order found in nematic, cholesteric, and smectic liquid crysals is provided in Figure 2.4.

2.3.2 Viscoelasticity in Isotropic Solutions

The effects of entanglement and confinement on semidilute and concentrated isotropic rod solutions have been described using a reptation model. In this model the rods are considered to be confined to a virtual tube of diameter a, which represents the aggregate of entanglement effects from the neighboring rods. The rod can translate (or "reptate") along its own axis with no hindrance, but cannot rotate or translate perpendicularly beyond the confines of the tube. In

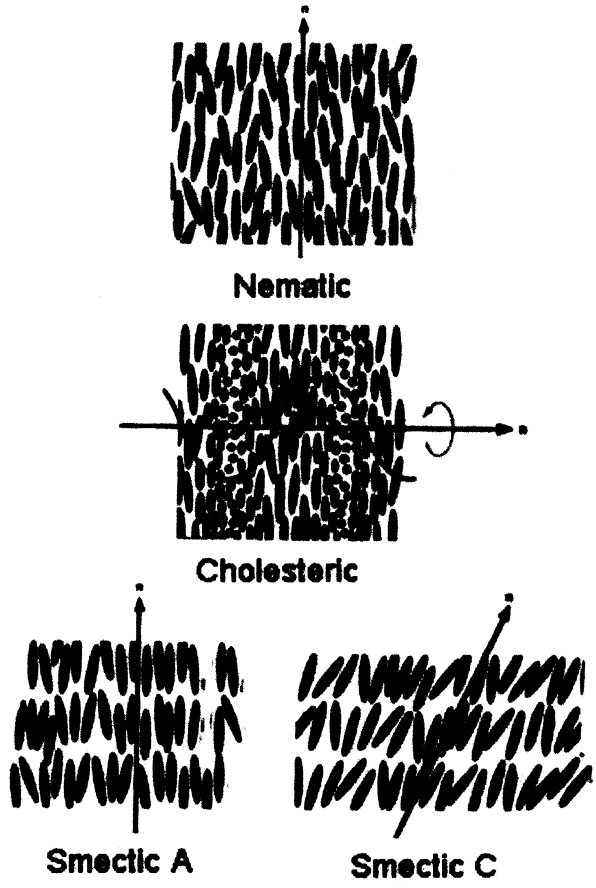

Figure 2.4: Representation of the primary classes of liquid crystalline ordering. Nematic liquid crystals align along a common dirctor **n**. Cholesteric liquid crystals align locally along a common director, but this director rotates along an axis perpendicular to it (in this figure the axis is defined as **n**, and the rotating director is perpendicular to **n**). Smectic liquid crystals exhibit positional as well as orientational ordering, consisting of ordered layers with the particles in each layer aligned along a common director for that layer, **n**. This director may either be common to all of the layers (type C) or different for each layer (type A). Reproduced from Donald and Windle (1992) without permission.

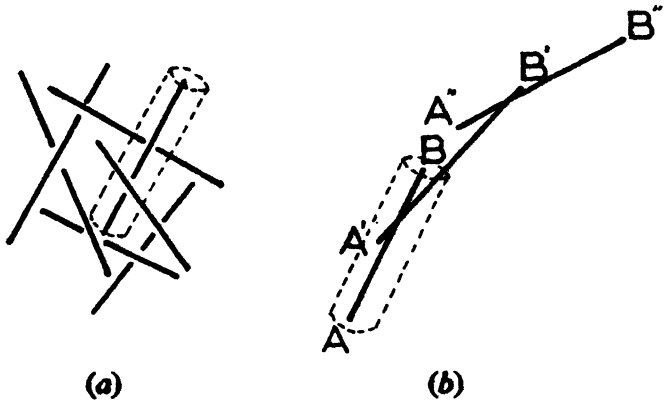

Figure 2.5: Representation of the reptation model in high concentration rigid rod solutions. (a) Neighboring rods forms a network that confines each rod to a virtual tube of a certain radius. Within this tube the rod is not able to translate perpendicularly or rotate beyond a short distance. (b) In order to change its orientation, a rod must leave its original confining tube by reptation - a combination of small rotations and translation along its axis. After a series of reptations, the rod will have completely left the original tube and found a new tube with a different, uncorrelated orientation. Reproduced from Doi and Edwards (1978) without permission.

order to change its orientation through rotation, the rod must translate a certain distance along its axis to find a new confining tube with a new orientation. This is illustrated in Figure 2.5 (Doi and Edwards, 1986, 1978).

Viscoelastic stress in polymer solutions, including rigid rod solutions, is a result of a combination of physical mechanisms. The stress in the system due to the application of a strain deformation can be separated into stress contributions from the solvent and from the polymers σ_S and σ_P. In the case of a Newtonian solvent, the solvent stress contribution is simply $\eta_s \frac{d\mathbf{v}}{d\mathbf{y}}$, where η_s is the solvent viscosity and $\frac{d\mathbf{v}}{d\mathbf{y}}$ is the velocity gradient induced during the application of strain. σ_P can further be separated into 5 components: these are the contribution from translational entropy, rotational entropy, bending stress within the polymers, stress from tension/extension in the polymer chains, and stresses due to excluded volume interactions between the polymers. Each stress component has a different free energy scale which determines the magnitude of its contribution to the instantaneous modulus $G(0)$, and each stress decays with its own characteristic time scale. As a result, the modulus measured over a given time scale is dominated by the strongest stress response that has not yet had time to decay (Morse, 1998).

In rigid rod solutions, σ_P is generally dominated by the effects of tension at very short time

scales, by the effects of rod curvature at intermediate time scales, and by the effects of orientational entropy at long time scales. For an oscillating strain with varying appied frequency ω, this implies that the high frequency response will be dominated by tension, intermediate frequencies will be dominated by curvature, and low frequencies will be dominated by orientation. The time scale below which tension is expected to dominate for dilute or loosely entangled solutions is either $\tau_{\phi L}$ or $\tau_{\|}$, which are the times needed for tension to be relieved by propagation of the force along the length of the rod (the distinction between the two time scales being whether or not entanglements occur frequently enough along this length to hinder the relaxation). The curvature stress is dominant on time scales shorter than either τ_L, which represents the time required for bending modes of length L to relax in an unentangled solution (where L is the length of the rod), or τ_{rep}, which represents the time required for a rod to relieve bending stress imposed by a bent **confining tube by reptating a distance equal to its own length; this distances it from each of the** entanglements which were formerly imposing the curvature. At all time scales longer than this, orientational entropy dominates the stress; this stress arises from the work done by the rods as they rotate back to an equilibrium distribution of orientations after that orientation distribution is changed by a strain.

The above relationships can be expected to hold for a system in which the rods are monodisperse in size and chemical structure. In practice, rods solutions are often polydisperse in length and diameter. The time scales described above will shift in value depending on size; in the case of many different rod populations existing in the solution it is likely that on any given time scale σ_P is composed of several different types of stress contributed by differently sized rods. Polydispersity in diameter and length is generally unavoidable in SWNT samples, in addition to the further complication of chirality polydispersity, which can lead to different chemical and electrical behavior.

Viscoelastic stress arising from rotational entropy in a rigid rod solution has been described by Doi & Edwards (see Doi and Edwards (1986)). For a rod solution undergoing oscillatory shear

strain with frequency ω, the complex shear modulus arising from rotational entropy is

$$G^*(\omega)=\frac{1}{i\omega}\left[\eta_s+G\tau_{\text{rot}}\left(\frac{1}{1+i\omega\tau_{\text{rot}}}+\frac{1}{3}\right)\right] \tag{2.5}$$

where τ_{rot} is the rotational relaxation time of the rods and G is the instantaneous shear modulus, which depends on the rod number concentration ν and the temperature T:

$$G=\frac{3}{5}\nu k_B T \tag{2.6}$$

The real and imaginary parts of G^*, which represent the elastic modulus G' and the viscous modulus G'', respectively, are

$$G'=G\frac{(\tau_{\text{rot}}\omega)^2}{1+(\tau_{\text{rot}}\omega)^2} \tag{2.7}$$

and

$$G''=\eta_s\omega+G\left[\frac{\tau_{\text{rot}}\omega}{1+\tau_{\text{rot}}\omega}+\frac{1}{3}\tau_{\text{rot}}\omega\right] \tag{2.8}$$

In the dilute concentration regime, in which the rotational motion of rods is not hindered by neighboring rods, the rotational relaxation time is

$$\tau_{\text{rot}}=\frac{\zeta_\perp L^3}{72k_B T} \tag{2.9}$$

In this regime, τ_{rot} is independent of concentration. In contrast, rotational motion in the semidilute concentration regime is hindered by confinement to a virtual tube created by neighboring rods, and the diameter a of this tube depends on concentration. In this case, rotational relaxation is carried out by a series of longitudinal movements of the rod in the confining tube, each of which allows a rotation through a small angle roughly equal to a/L. The rotational relaxation

time of the rod is then given by

$$\tau_{\text{rot}} = \frac{\zeta_{\perp} L^3}{72 k_B T} \left(\frac{L}{a}\right)^2 \tag{2.10}$$

The confinement length a for a given rod in a semidilute or concentrated isotropic solution can be estimated by considering the number of other rods which intersect a virtual cylinder of radius r around that test rod, denoted $N(r)$. This number will be determined by the length of the rod in question, the number concentration of rods in the system, and the orientation distribution of the rods. In the most general case, for a set of rods with a length probability distribution $P(L)$, number concentration ν, and orientation distribution $\Psi(\mathbf{u})$, the number of rods intersecting a cylinder of radius r around a test rod of length L is

$$N(r) = \frac{1}{2} \int\int\int \Psi(\mathbf{u}') \nu P(L') L' \, |\, \mathbf{u}' \cdot \mathbf{n} \,|\, \mathrm{d}\mathbf{u}' \mathrm{d}L' \mathrm{d}A \tag{2.11}$$

where the factor of $\frac{1}{2}$ is included to account for the fact that most rods pass through the cylinder twice (Doi and Edwards, 1986; Marrucci and Gizzuti, 1983). The integration accounts for all possible lengths & orientations of the intersecting rods over the surface area of the virtual cylinder. In the case of an isotropic solution,

$$N(r) = \frac{\nu \pi r L}{2} \int P(L') L' \mathrm{d}L' \tag{2.12}$$

The confinement length at a given concentration is determined to be the radius at which the number of rods intersecting the cylinder is on the order of 1, $N(a) \simeq 1$. In the simple case of monodisperse rod length,

$$a = \frac{\alpha}{\nu L^2} \tag{2.13}$$

The unknown numerical factor α represents the uncertainty about the number of rods that must intersect the virtual cylinder in order to truly cage the rod within that cylinder; one or two entan**glements would certainly not be enough to create an effect equivalent to that of a solid confin-**

ing tube. Experiments on rod solutions have indicated that α is approximately 30 (Teraoka and Hayakawa, 1989; Larson, 1999).

If rod-like molecules are modeled more realistically as slightly flexible chains rather than infinitely stiff rods, it can be seen that the effect of confinement on the behavior of the rod depends on the entanglement length a. The flexibility of a rod-like chain results in undulations along the contour length of the rod; the wavelength of these undulations is determined by the stiffness of the rod, which is in turn related to the persistence length. If the contour length of the rod-like chain is greater than the length scale

$$\lambda = \sqrt[3]{L_p a^2} \tag{2.14}$$

then the size of the confining tube is comparable to the transverse displacement due to these contour fluctuations (Odijk, 1983). In this case, the flexibility of the rod-like chain alters its behavior from that which would be expected for a perfectly rigid rod; escape from a confining tube will be easier due to the ability of the rod to bend slightly and find pathways through which it can reptate. In this case, the rotational relaxation time of the rod is

$$\tau_{\text{rot}} = \frac{\zeta_\perp L^2 L_p}{12 k_B T} \tag{2.15}$$

The onset of this tight level of entanglement creates a third concentration regime in terms of the calculation of rotational relaxation time τ_{rot}; effectively, flexibility puts a lower bound on how slowly a rod is able to relax, and this relaxation behavior will be observed at higher concentrations, for which (2.10) > (2.15). The transition to this flexibility-enabled rotational relaxation behavior has recently been observed in individual HiPco SWNTs confined in porous media (Fakhri *et al.*, 2010).

2.3.3 Rigid Rod Percolation

The transition from fluid-like to solid-like behavior in polymeric solutions occurs when the concentration becomes high enough for a percolated network to form throughout the system, in

which the movement of the constituent polymers is more or less arrested and which possesses mechanical properties reminiscent of a solid material, such as high elasticity and observable yield stress. The transition to a percolated system can generally be observed through a dramatic change in the mechanical properties of the material, an increase in electrical conductivity (if the dispersed species is conductive), or a decrease in the translational diffusivity of the constituent particles/molecules.

Rigid rod systems can be found in a wide variety of solvents, with rodlike dispersants spanning four orders of magnitude in length and three orders of magnitude in aspect ratio. Despite this great variety, it has been observed that the fundamentally similar geometries present in rod solutions give rise to analogous behavior at all length scales. There are 4 key variables that determine the microstructure and dynamics of rod solutions within the domain of colloidal dispersions. **These are the aspect ratio of the rods, the rod flexibility, the concentration of rods in the fluid, and the strength of attractive interactions between the dispersed rods** (Solomon and Spicer, 2010).

The nature of the transition to solid-like behavior in rigid rod dispersions is highly dependent on the last variable, and can fall on a continuum between two limiting cases, which are depicted in Figure 2.6. In the limit of small attractive interactions between rods, $U \ll k_B T$, the dispersion remains homogeneous at length scales greater than the size of a single rod; in this case, at a certain critical concentration, excluded volume interactions result in the formation of a jammed glass of entangled rods. This case is characterized by an abrupt transition to arrested structure dynamics once the critical percolation concentration has been reached. A liquid crystalline phase is generally expected to form at concentrations above this in response to the decreasing degree of translational freedom possessed by the rods in the crowded system.

If the rods attract one another strongly, with $U \geq k_B T$, they tend to form a connected fractal structure referred to as a rod gel. One consequence of this is that the network structure becomes heterogeneous on scales greater than the length of the rods due to wide spacing of rods in the **network: the rods will aggregate into fractal clusters with empty fluid between them, and into** branching structures within those clusters. Another feature of fractal network formation is a

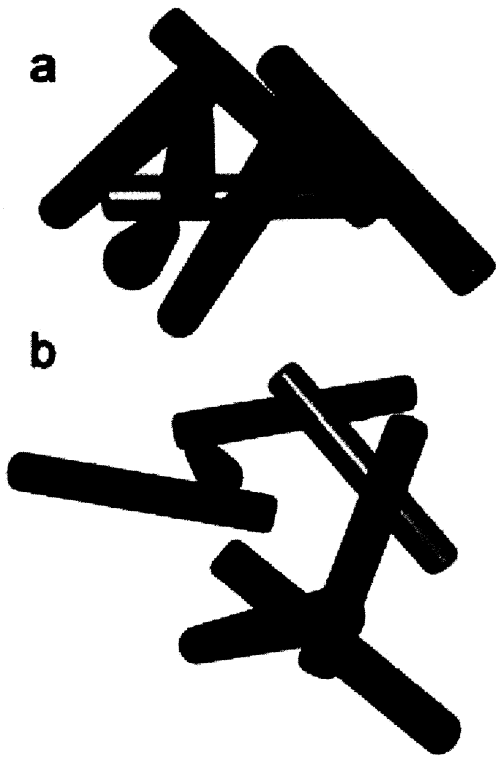

Figure 2.6: Schematic of rods forming (a) a homogeneous glass network or (b) a fractal gel. In the former, rods interact primarily through excluded volume interaction, and form a percolated network when the system becomes crowded enough to jam; each rod has contact with many of its neighbors. In the latter, attractive forces cause the SWNTs to transition to arrested behavior after forming only two or three contacts with neighboring rods, resulting in a more open and inhomogeneous network. Reproduced from Solomon and Spicer (2010) without permission.

more gradual onset of solid-like behavior with concentration, because the dynamics within the fractal network slow down incrementally as the network forms more connections. Because of the heterogeneity of fractal networks, a continuously connected fractal gel can arise in rod systems with shorter aspect ratios and/or at lower concentrations than would be required for the formation of a rod glass. Rod systems with intermediate values of U are expected to exhibit behavior between the two extreme cases of rod glass and rod gel.

Chapter 3

Materials and Methods

This chapter provides an overview of the experimental methods used in this study as well as the materials used to create and then test the samples. It provides a brief discussion of the practical challenges faced when dealing with strong acid samples, and also an analysis of the experimental limitations which determine the fequency, strain, and SWNT concentration ranges accessable by experiment.

This study was performed using solutions of HiPco SWNTs in two superacids: chlorosulfonic acid ($ClHSO_3$) and fuming sulfuric acid (H_2SO_4 containing excess SO_3, in which no H_2O is present). Due to the nature of these superacids, the materials and procedures employed had to be carefully selected in order to avoid health risks, damage to equipment, and degradation of the quality of the solutions themselves. Both acids react readily with ambient atmospheric moisture, and this reaction results in a dilution of the acid which, in turn, alters the attractive potential of dissolved SWNTs. In addition, exposure of either $ClHSO_3$ or fuming H_2SO_4 to atmospheric moisture results in the release of acidic fumes (HCl and SO_3 gas, respectively) which are hazardous to inhale and can cause corrosion in nearby materials and apparatus. For these reasons, the solvents and solutions used in this study needed to be mixed, handled, and tested within enclosed glove box environments flushed with moisture-free air. The materials employed to work with the acids had to be those with little or no susceptibility to corrosion in $ClHSO_3$ and H_2SO_4, such as

glass, PTFE, and 316 stainless steel. Apart from minor changes, the methods used in this study are the same as those that have been described in Banzola (2008).

3.1 Preparation of Solutions

The SWNTs used in this study were produced from the high-pressure carbon monoxide (HiPco) process and purified to remove residual iron catalyst (Carver *et al.*, 2005; Xu *et al.*, 2005). These SWNTs are polydisperse in both diameter and length. 120% H_2SO_4 (i.e., H_2SO_4 containing 20% excess SO_3 by mass,), 96% H_2SO_4, and 99% $ClHSO_3$ were used as received from Sigma Aldrich.

In order to prepare a superacid solution with a lower protonating strength than 120% H_2SO_4, 102% H_2SO_4 was prepared by mixing 120% H_2SO_4 with 96% H_2SO_4. Volumes for mixing were calculated based on estimated SO_3 and water content, respectively, of the as-received materials, and the SO_3 content of the final mixture was determined by titration with NaOH; further mixing was performed until the desired SO_3 content was achieved. Mixtures of $ClHSO_3$ and 102% H_2SO_4 were also prepared to serve as solvents of intermediate strength. In order to prepare these solutions, 102% H_2SO_4 prepared as described above was mixed with 99% $ClHSO_3$.

SWNT solutions were prepared by mixing acids with dry SWNTs in glass vials within a glove box flushed with desiccated air (dew point -50 °C). Volume fractions of SWNTs were calculated with the assumption of a SWNT density of 1450 kg/m^3, which is typical of HiPco SWNTs (assuming that acid does not fill the inside of the SWNTs) (Davis, 2006). The solutions prepared for this study were all below 1 vol% SWNT, and as such all had viscosities suitably low for stir-bar mixing to be effective (under 100 Pa s at a shear rate of 0.1 s^{-1}, with lower viscosity at higher shear rates due to the shear-thinning nature of SWNT solutions). Solutions were mixed on magnetic stir plates using Teflon-coated stir bars. Solutions of SWNTs in $ClHSO_3$ were mixed for 24 hours and solutions in 102% H_2SO_4 or in mixtures of the two acids were mixed for 72 hours to ensure homogeneous distribution of the SWNTs.

3.2 Microscopy

Light microscopy of acid solution samples was performed on a Zeiss Axioplan microscope using microscope slides and cover slips dried beforehand in an oven. Microscope slides were assembled in an anhydrous glove box, and the edges of the cover slips were sealed with tape to prevent moisture from compromising the sample.

Polarized microscopy was performed in transmission mode through the use of independently rotatable polarizing filters placed in the light path before and after the sample (termed the polarizer and analyzer, respectively). This technique exploits the optical properties of anisotropic materials, in which the refractive index differs for light polarized in different planes - such materials are known as birefringent materials. Polarized light that is transmitted through a birefringent sample is split into two components with polarizations parallel and perpendicular to the optical axis of the sample. When the light subsequently passes through a second polarizing filter, only the components of these two waves which are parallel to this polarizer's axis will pass through. If the polarizing filters before and after the sample are oriented with optical axes orthogonal to one another, then the only light that is able to pass to the objective is that which has been re-oriented by birefringent areas in the sample. This technique was employed to visualize aligned liquid crystalline domains in SWNT solutions.

3.3 Rheology

3.3.1 Experimental Setup

Rheological measurements on $ClHSO_3$ solutions require careful treatment of the sample due to the highly corrosive nature of the acid and the fact that it reacts readily with ambient moisture to produce HCl gas. Methods which have been previously developed for rheological measurements on SWNT/102% H_2SO_4 samples (Davis *et al.*, 2004; Davis, 2006) are not effective when $ClHSO_3$ is present in the solution. Instead, the apparatus and testing methods used in this study are similar to those described in Banzola (2008). Measurements were performed within a glove box flushed

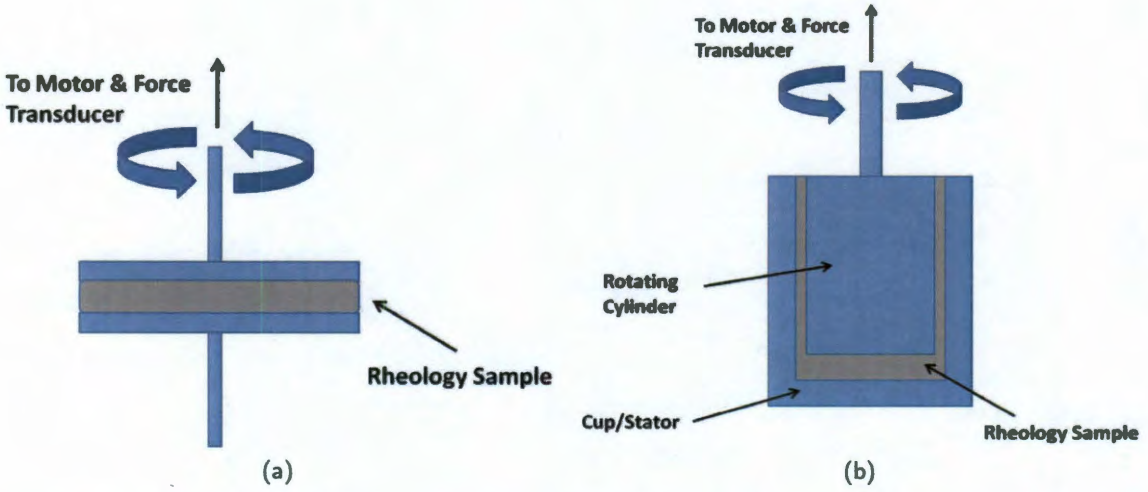

Figure 3.1: (a) Schematic of a parallel-plate rheometer testing geometry. (b) Schematic of a concentric-cylinder couette rheometer testing geometry. On a stress-controlled rheometer such as the AR 2000ex, the geometry is rotated and coupled to a force transducer by the same shaft, i.e., the rotating part doubles as the stress sensor.

with dessicated air (dew point -50 °C) using an AR 2000ex stress-controlled rheometer (TA Instruments, New Castle, DE). Testing fixtures were made of stainless steel 316 to avoid corrosion. Two testing geometries were used in this study: a single walled concentric-cylinder couette was used for solutions having a concentration of 4000 ppm or less, and a 40 mm smooth-faced parallel plate geometry was used for solutions with concentrations higher than this. Another testing geometry, a double-walled couette, was tried for the purpose of extending this study to lower concentration solutions, but had to be abandoned for reasons discussed below. Thorough descriptions of these testing geometries can be found in Macosko (1994). Prior to all experiments, the testing geometries and vials containing the samples were sealed in the glove-box, which was then flushed with dry air overnight.

During the course of this study, it was observed that the body of the rheometer had begun to suffer corrosion. Although the air that is flushed through the glove box has a dew point of -50°C, corresponding to a relative humidity level of 1-2%, this trace amount of moisture is enough to react with $ClHSO_3$ to produce a small amount of HCl gas. In addition to this, the cleaning procedure that had been developed for this kind of experiment, as described by Banzola (2008), was not completely suitable for preventing corrosion. This procedure was as follows: the user

would transfer as much acid solution as possible from the testing geometry to its original glass container, then dilute the acid remaining in the stainless steel testing geometry with chloroform before opening the glove box and exposing it to the outside air in order to retrieve the geometry for cleaning. The act of diluting the remaining acid with chloroform routinely produces visible fumes, possibly HCl gas produced by a reaction of the acid with trace amounts of water in the chloroform. Although the fumes produced by trace atmospheric moisture and those produced during the cleaning procedure are slight compared to the fumes released by the acid in open air, they were still enough to cause visible corrosion to the exposed surfaces of the rheometer body as well as damage to the electrical components.

To avoid further damage to the rheometer, two new procedures were developed. First, a Plexiglas cover was manufactured to enclose the rotor and acid solution during testing, without forming an air-tight seal. An air line in the side of this Plexiglas piece is connected to an acid trap and air pump outside of the glove box. The air pump applies a slight suction in the area immediately above the solution, drawing away any HCl fumes that are produced in the course of the test. The stainless steel couette geometry is pictured in Figure 3.2, with and without the new Plexiglas cover. Second, the cleaning procedure used after the conclusion of each test was altered: instead of the acid being recovered and the geometry flushed with chloroform, the geometry is now detached from the rheometer shaft and, still containing the acid, placed into a glass beaker, which is then covered with parafilm. Once the beaker is sealed, the glove box can be opened, and the beaker removed to another glove box or to a fume hood where the geometry can be cleaned. This method affords minimal opportunity for the solution to produce corrosive fumes during cleaning since it avoids mixing the acid with chloroform; it also avoids the previously necessary step of separating the two halves of the testing geometry to move the acid back into its original vial, which was observed to increase fuming due to the temporarily increased exposure of the acid.

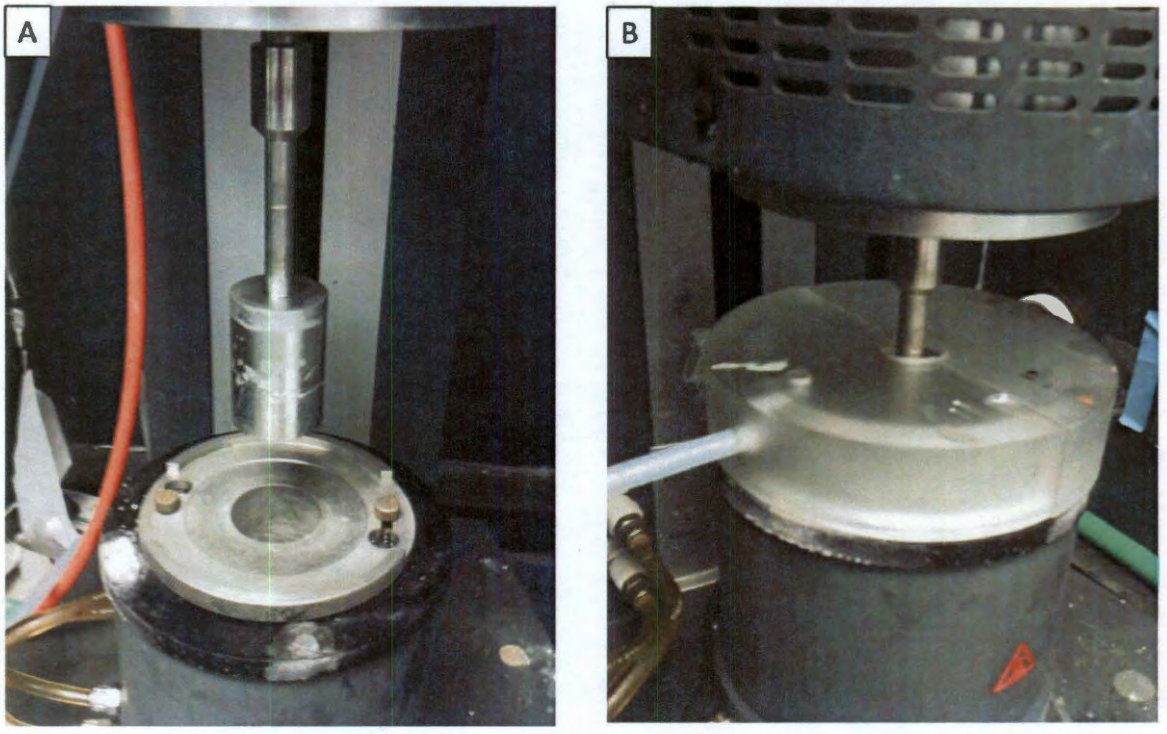

Figure 3.2: (A) Concentric cylinder couette geometry mounted on the AR 2000ex. Although the pieces are made from stainless steel 316, some corrosion and discoloration has appeared on the surfaces due to repeated use. (B) The same couette geometry, with the addition of a new Plexiglas cover. The cover consists of two separate pieces which can be put into place after the rotor has been lowered into the cup, with a central opening that allows the rotor to turn. An air line in the side of one piece can be used to pull HCl fumes into an acid trap, limiting the amount of acid vapor released into the glove box and avoiding further corrosion of the rheometer or testing geometries. This cover was designed to fit over the 40 mm parallel plate testing geometry as well.

3.3.2 Dynamic shear tests

Dynamic (oscillatory) shear tests provide a measurement of the viscoelastic properties of a fluid. In an oscillatory shear test the testing geometry is rotated back and forth within the fluid in a sinusoidal oscillation of prescribed frequency and strain amplitude. The stress response of the fluid is a corresponding sinusoidal curve with the same frequency, shifted by a phase angle δ from the strain curve. This stress curve can be broken into two components: one in phase with the strain and one shifted by $\frac{\pi}{2}$. These components represent the elastic and viscous stress responses of the fluid, respectively. If the amplitude of the strain oscillation is small enough, the stress depends linearly on the strain amplitude; i.e., the test probes the linear viscoelastic response of the fluid. For strains in this linear viscoelastic regime, the viscoelastic properties of the material can be measured without disrupting the material's structure. Two types of dynamic shear tests were used in this study: strain sweep measurements, in which frequency is fixed and the strain amplitude is varied, and frequency sweep measurements, in which strain is fixed and frequency is varied.

A strain sweep measurement is performed by fixing a frequency and then choosing a range of strain amplitudes over which the measurement should be taken (Mezger, 2006). For strain values within the linear viscoelastic regime the elastic and viscous moduli of the solutions are independent of strain amplitude; thus this measurement can be used to determine the critical strain, γ_c, below which a solution exhibits linear viscoelastic behavior. γ_c can be defined as the strain at which either G' or G'' deviates from its strain-independent value by more than 5%, indicating the onset of non-linear behavior. Strain sweep tests can also be used to determine which strain amplitudes will produce a torque too small to be measured at a given frequency. In this study, strain sweep measurements were used to find γ_c and to determine a suitable strain amplitude value for any frequency sweep tests performed on the same solution. In general, the strain amplitude chosen for subsequent frequency sweep tests is the just below γ_c, because it is the strain which will produce the largest stress response while maintaining linear behavior. This maximizes the range of frequencies for which subsequent frequency sweep measurements will have a response that is greater than the torque sensitivity limit of the rheometer. Figure 3.3

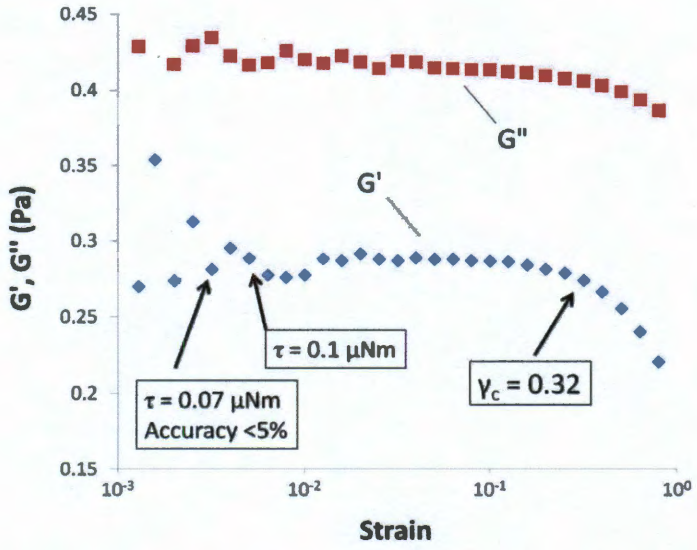

Figure 3.3: G' and G'' for a solution of 5200 ppm SWNT solution in $ClHSO_3$. The critical strain which represents the limit of the linear viscoelastic region is $\gamma = 0.32$; at strains higher than this, both G' and G'' deviate significantly from their strain-independent values. The data below this strain value fall within 5% of a constant average value so long as the measured torque is above 0.07 μNm. 0.1 μNm is the nominal sensitivity limit of the rheometer.

displays the results of a strain sweep test on SWNTs at a concentration of 5200 ppm in $ClHSO_3$. In this case $\gamma_c \sim 0.32$ (32%), at which strain G' departs from a constant value. The small torque value measured by the instrument at low strain values is beyond the sensitivity of the instrument, as discussed in § 3.3.3.

Frequency sweep measurements are performed by keeping the strain amplitude fixed, and measuring viscoelastic properties over a range of frequencies (Mezger, 2006). By probing the response of the fluid to strains applied at different frequencies this test essentially probes the relaxation mechanisms acting in the fluid over different time scales, and therefore different length scales. Thus, information about the physical structure present in the fluid can be gained from studying the frequency-dependent elastic and viscous moduli, $G'(\omega)$ and $G''(\omega)$. The viscous modulus of the solution has two additive components: the contribution from the SWNTs and the contribution from the superacid, which is a Newtonian fluid with viscous modulus $\eta\omega$. It is often more informative to consider only the contribution of the SWNTs to the viscous modulus, $G''_{SWNT}(\omega) = G''(\omega) - \eta\omega$. Figure 3.4 displays sample data collected from a frequency sweep

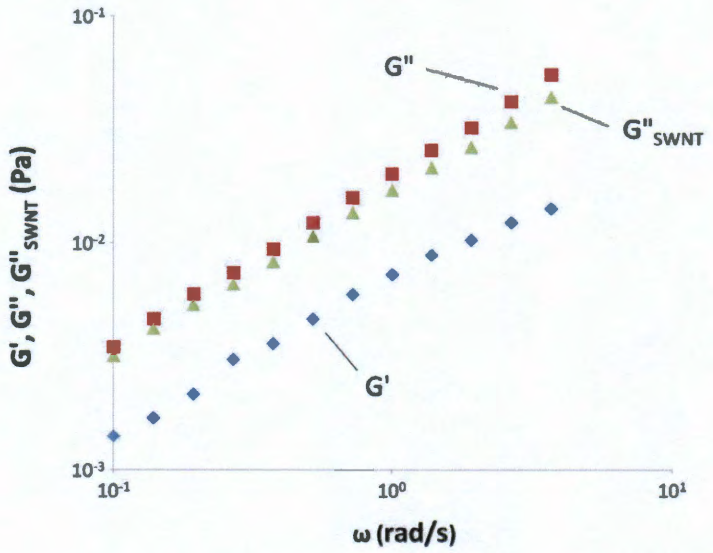

Figure 3.4: Viscoelasticity data obtained from a frequency sweep experiment on a solution of 600 ppm SWNTs in $ClHSO_3$. The experiment measures G' and G'' as a function of ω, **with a fixed applied strain** γ (in this case, $\gamma = 0.1$). Also plotted is G''_{SWNT}, which represents the contribution of the SWNTs to the viscous modulus with the contribution of the solvent removed.

measurement on 600 ppm SWNTs in $ClHSO_3$. A comparison between G'' and G''_{SWNT} shows that the solvent contribution to the viscous modulus is small compared to the contribution of the SWNTs.

3.3.3 Experimental Limitations

The range of frequencies over which the collection of viscoelastic data was attempted for this study for this study was 0.1 rad/s to 100 rad/s; data collection at lower frequencies requires a longer data collection time, so 0.1 rad/s was chosen as a practical lower limit to avoid prohibitively long experiment times. However, the accessible experimental range was actually much narrower than this for SWNT solutions with concentrations lower than 0.4 vol% due to two different effects, one of which placed and upper limit and one a lower limit on the frequencies at which useful data could be obtained. At lower concentrations (below about 0.05 vol%) the combination of these two effects, described below, caused the accessible experimental range to disappear entirely.

One of these problems is the lack of reliability in dynamic measurements made at sufficiently low torques. The determination of G' and G'' in the course of a dynamic shear test depends on the amplitude of the sinusoidal torque response (from which the sinusoidal stress curve is calculated) and the phase angle δ, which are determined by fitting a sinusoidal curve to the torque data measured over the course of the oscillation. The lower the torque response of the sample, the greater the noise in the data and the greater the error in the sinusoidal fit. The resulting uncertainty in the amplitude and phase angle of the torque curve translates to error in the measurement of G' and G''. The AR 2000ex is rated to measure quantities accurately (within 5%) so long as the measured torque is above 0.1 μNm. In practice, this level of accuracy can usually be obtained even at slightly lower torques - in Figure 3.3, arrows are drawn indicating the point at which the measured torque amplitude falls below 0.1 μNm and the point at which the measurement begins to deviate by more than 5% from the average constant value, which in this case happens below a torque amplitude of 0.07 /muNm.

If the component of oscillatory torque representing the elastic response is too low, the instrument attempts to fit an "in phase" curve to the noise, and reports a value of 0.03 μNm for the elastic torque. If the geometry being used is the concentric cylinder couette, this results in a measurement of 3-4 x 10^{-3} Pa. This "noise" level of elasticity is reported even for Newtonian liquids, and represents an absolute lower limit on the magnitude of elastic modulus that can be measured, even inaccurately, with this instrument.

The second major source of error, which placed an upper limit on the range of measureable frequencies for low viscosity solutions, arose from the inertia of the testing geometry. The AR 2000ex is a stress-controlled rheometer, and as such it carries out the rotation of the test geometry using the same shaft to which the force transducer is coupled; this provides the option of applying a specified stress to the fluid, rather than inducing a specified shear rate. Unfortunately, the fact that the rotor doubles as the stress probe creates a source of experimental error in dynamic shear tests: due to the rotational inertia of the rotor, a significant torque must be applied to keep the rotor turning back and forth sinusoidally. This inertial torque is $I\omega^2$, where I is the moment of inertia, and it grows quadratically with increasing frequency. The AR 2000ex software

records the moment of inertia of the rotor during calibration and has a function to account for this inertial torque; in addition, the rotational response of the rotor can be mapped and recorded using a mock test at a given set of frequencies to serve as a baseline from which fluid stress can be distinguished during an actual test. However, in the case of high frequencies and/or low viscosity solutions it is possible that the torque due to the rotor inertia will be so large compared to the torque from the sample that the software cannot distinguish the sample response at all. When this occurs, the data collected become meaningless.

In dynamic shear frequency sweep measurements of SWNT solutions in $ClHSO_3$, the inertial torque of the rotor was observed to dominate the measurement of $G'(\omega)$ and $G''(\omega)$ at frequencies lower than 100 rad/s if the concentration of the solution is lower than around 0.4 vol%; at concentrations higher than this, the moduli of the solutions are high enough that they provide enough torque to avoid the problem. The deviation from true measurement of the solution properties begins at lower frequencies for solutions with lower SWNT concentration. Below a SWNT concentration of around 600 ppm in $ClHSO_3$, no trustworthy viscoelastic data could be obtained due to the combined effect of intertial torque at high frequency and low sample torque at low frequencies.

Figure 3.5 displays $G'(\omega)$ curves for three concentrations of HiPco SWNTs in $ClHSO_3$: 3600 ppm, 600 ppm, and 120 ppm. In each curve, there is a concentration at which the data become meaningless, marked by a steep decline in G' (the value reported by the software actually becomes negative). The frequency at which this occurs varies with concentration. The higher the concentration of SWNTs in the solution, the greater the viscoelastic stress induced in the fluid in response to strain; thus for higher concentrations one can reach higher frequencies before the intertial torque of the rotor becomes large enough to overwhelm the measurement. For the 120 ppm solution, viscoelastic stress from the fluid could be measured below 1 rad/s without interference from the rotor, but at these frequencies the torque measurement from the fluid was well below the measurement range of the instrument and the measured G' data was dominated by noise. This concentration is therefore outside of the experimentally accessible range; it is a part of a low concentration regime for which the effects of the two measurement problems overlap.

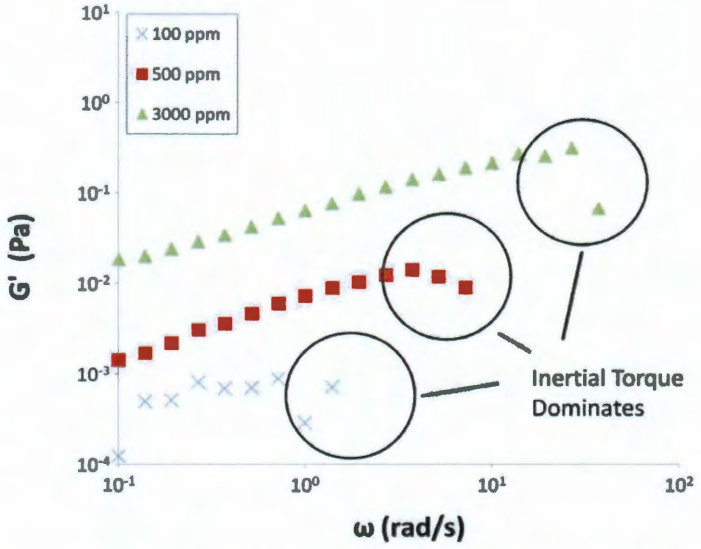

Figure 3.5: $G'(\omega)$ data obtained in frequency sweep experiments for 3600 ppm, 600 ppm, and 120 ppm SWNT solutions in $ClHSO_3$. Measurements were taken on a stainless steel concentric-cylinder couette. Above a certain frequency in each case the measured torque values are dominated by the inertial torque of the steel rotor, leading to a strong deviation in the measurement. This deviation occurs at lower frequencies for fluids with lower complex viscosity, due to their proportionally smaller sample torque response. Data curves appear to end prematurely on the log-log plot due to the measurement of $G'(\omega)$ becoming negative, an indication that the data are no longer physically meaningful. For the lowest concentration shown here, 120 ppm, the data that are not dominated by inertial torque are instead below the torque sensitivity limit of the rheometer, leading to a G' measurement that is dominated by noise; for this reason no useful data could be gathered for this solution. Concentrations around 600 ppm were the lowest viscosity solutions that could be tested meaningfully with the AR 2000ex.

In order to extend the range of solution concentrations that could be investigated in this study, a custom-made testing geometry was obtained. This geometry was a double-walled concentric cylinder couette in which the rotor is a hollow cylinder with an open face at the bottom, which is inserted into a sample that is contained within an annular ring in the cup/stator; thus the sample is in contact with the rotor along both its inner and outer surface. The custom geometry obtained for our acid work included a cup/stator made of stainless steel 316 and a rotor made of aluminum, in order to reduce the moment of inertia of the rotor compared to one made of stainless steel. In order to prevent corrosion of the aluminum in our acid solutions, the rotor surface was coated with a PTFE (Teflon) film. It was hoped that this geometry would increase the maximum measureable frequency for low concentration solutions because of its reduced moment of inertia, while also increasing the torque measured from the sample because of its increased surface area, thereby reducing the frequency at which the torque of the solutions becomes too low for the rheometer to detect.

Tests performed using this geometry did not significantly increase the upper limit of the frequency range; the moment of inertia of the aluminum rotor was not lower than that of steel by a large enough margin to make a difference. Use of the double-walled couette geometry did however extend the measureable range of 600 ppm solutions to lower frequencies. Unfortunately the Teflon layer deposited on the aluminum rotor was not impermeable to the acid, and after only a few tests the Teflon coating began to detach and peel away. Thus, testing with this rotor had to be abandoned. A double-walled couette rotor made of stainless steel, however, would be a suitable replacement and has the prospect of extending the experimental range to lower concentrations.

Chapter 4

Effect of Solvent Strength and Concentration on Microstructure

The first part of this chapter describes the results obtained from dynamic shear measurements of SWNTs dissolved in $ClHSO_3$ acid, and discusses those results in the context of experiments that have been performed in the past on HiPco SWNTs in both $ClHSO_3$ and 102% H_2SO_4. The goal of this combined set of experiments was to investigate how the SWNT microstructure changes with concentration in the case of an athermal solvent ($ClHSO_3$) and in the case of a weak solvent (102% H_2SO_4). The chapter proceeds to discuss the match between rigid rod solution models and the data obtained at low concentrations, as well as the key differences in percolation behavior found in the two acids at intermediate concentrations. Lastly, it describes the results of dynamic shear measurements performed on SWNT solutions at a fixed concentration in superacid solvents with a range of protonating strength, demostrating how microstructure varies continuously with inter-SWNT attractive potential.

4.1 Varying Concentration

In the course of the current study, rheological tests were performed on solutions with SWNT concentrations between 600 ppm and 8000 ppm by volume. These results are part of a larger

picture built from several experimental studies, which reveals the microstructure and phase behavior of SWNTs in superacids. The rheological data obtained in this study, taken together with the results of a previous study on SWNT/$ClHSO_3$ solution rheology performed by Marco Banzola, provide a map of the viscoelastic properties of SWNTs in $ClHSO_3$ across a broad concentration range (600 ppm to 12 vol%) (Banzola, 2008). This data can be compared to the corresponding map derived from a similar set of experiments that were carried out on HiPco SWNTs in 102% H_2SO_4 acid by Virginia Davis (Davis, 2006). The structure of SWNT/acid solutions has been studied using other methods, such as centrifugation-induced phase separation and differential scanning calorimetry. These experiments investigated the phase boundaries between isotropic, biphasic, and liquid crystalline SWNT solutions as a function of both concentration and superacid strength. In this section, the combination of these experiments is synthesized to draw conclusions about the effect of inter-nanotube attraction on the development of liquid crystalline structure and percolated networks, and the agreement between experiment and rigid rod theory, in SWNT/superacid solutions.

6 SWNT volume concentrations were tested in this part of the study: 600 ppm, 1200 ppm 3700 ppm, 5200 ppm, 7500 ppm, and 8000 ppm. Tests of 120 ppm and 370 ppm were also attempted, but these concentrations were outside of the range in which viscoelastic response could be measured with the AR 2000ex Rheometer.

4.1.1 Phases of SWNT solutions

Phase separation experiments indicate that the transition from isotropic SWNT solution to biphasic SWNT solution (containing some liquid crystalline domains) occurs at approximately 3000-4000 ppm in $ClHSO_3$ (Davis *et al.*, 2009). The concentration range investigated here therefore includes both isotropic and biphasic solutions. The previous experiments on SWNTs in $ClHSO_3$ to which the data will be compared were performed on solutions with higher concentrations ranging from 1.2 vol%, which falls in the biphasic regime, to 12 vol%, which is believed to be fully liquid crystalline (Banzola, 2008).

102% H_2SO_4 acid has less protonating ability than $ClHSO_3$. As a result, SWNTs in 102% H_2SO_4 experience a weak mutual attraction (Parra-Vasquez *et al.*, 2010; Green *et al.*, 2009). This leads to two readily observable differences from the behavior of SWNTs in $ClHSO_3$. One difference is that in 102% H_2SO_4, liquid crystalline domains appear at a much lower concentration, and as a result the biphasic regime extends over a broader range of concentrations than it does in $ClHSO_3$ (3 decades instead of 4) (Davis *et al.*, 2009). Birefringent liquid crystalline regimes have been observed in light micrographs of SWNT/102% H_2SO_4 solutions at concentrations as low as 100 ppm. Experiments on the phase separation of isotropic and liquid crystalline SWNTs due to centrifugation and an analysis of these results using Onsager theory have indicated that the onset of the biphasic region in 102% H_2SO_4 may actually be much lower than this; it is possible that even the lowest concentrations tested in previous rheological studies, 30 ppm, contained some liquid crystalline SWNTs (Green *et al.*, 2009).

The other difference caused by the increased inter-SWNT attraction is in the morphology of the liquid crystalline domains themselves. In $ClHSO_3$ the liquid crystalline domains take the form of elongated drops reminiscent of nematic tactoids; in H_2SO_4 the liquid crystalline phase takes the form of extremely long and thin strand-like domains which have been termed "spaghetti domains" (Davis *et al.*, 2004). One possible explanation for the elongated shape of these domains is that the increased attractive forces between SWNTs greatly increases the elastic forces which prevent mis-alignment of the SWNTs within the domain; this elasticity acts against the forces of surface tension that would otherwise drive the domain to have a more spherical or tactoidal shape, requiring misalignment of the SWNTs near the curving interface. These two key microstructural differences - the changes in the number and the shape of liquid crystalline domains - cause major differences in the viscoelastic behavior and the percolation of SWNTs in the two solvents.

The viscoelasticity measurements of SWNTs in 102% H_2SO_4 to which the results of this study will be compared were performed on solutions ranging from 30 ppm, which is biphasic, to 11 vol%, which is fully liquid crystalline (Davis, 2006).

4.1.2 Experimental Results

The results of strain sweep measurements performed on solutions in $ClHSO_3$ between 600 ppm and 8000 ppm are shown in Figure 4.1; part (a) plots G' and part (b) plots G''_{SWNT}. These measurements were performed at a fixed frequency of 3.14 rad/s (note: this value, not π, is the exact frequency input during test setup). For measurement at lower values of strain amplitude, the samples have a lower stress response to the oscillatory applied strain; measurements at sufficiently low strains resulted in a torque below 0.1 μNm, below the torque sensitivity limit of the instrument, and have been omitted from the plots. A strain sweep test was performed on 1200 ppm SWNTs in $ClHSO_3$, but that test was performed at a frequency of 1.5 rad/s; therefore although those the results were useful for determining critical strain for that concentration, the G' and G''_{SWNT} curves for that concentration cannot be directly compared to the other results.

Two general trends can be discerned from the results of these strain sweep tests. The first is that the magnitude of G' relative to that of G''_{SWNT} increases as the SWNT concentration increases, indicating a greater prominence of elastic stress with a greater loading of SWNTs. This is made clearer in Figure 4.2, which plots the loss modulus $\tan(\delta)$ vs. strain calculated using the above results. Note that the value plotted here is a loss modulus calculated using G''_{SWNT}, the viscous modulus contributed only by the SWNTs in the solution, rather than the full G''. The other noticeable trend is that the value of critical strain, γ_c, decreases with increasing concentration. γ_c can be determined by observing the strain value at which either G' or G''_{SWNT} begins to diverge from a constant value. The value of G' for 600 ppm solution, for example, is constant until around 40% strain, whereas at the highest concentrations γ_c decreases to around 2%. This decrease indicates that at higher SWNT concentrations, the structures formed by the SWNTs are sensitive to disruption from increasingly small shear strains.

These two trends, namely the increased dominance of elastic stress and the decrease of critical strain with increasing SWNT concentration, can be considered in the broad context of all the viscoelastic data collected in the past for HiPco SWNTs in 102% H_2SO_4 and at higher concentrations in $ClHSO_3$. Figure 4.3 plots the value of γ_c obtained from these tests as a function of SWNT concentration in both acids. In $ClHSO_3$, γ_c exhibits a plateau value of 40% from 600 ppm to 3700

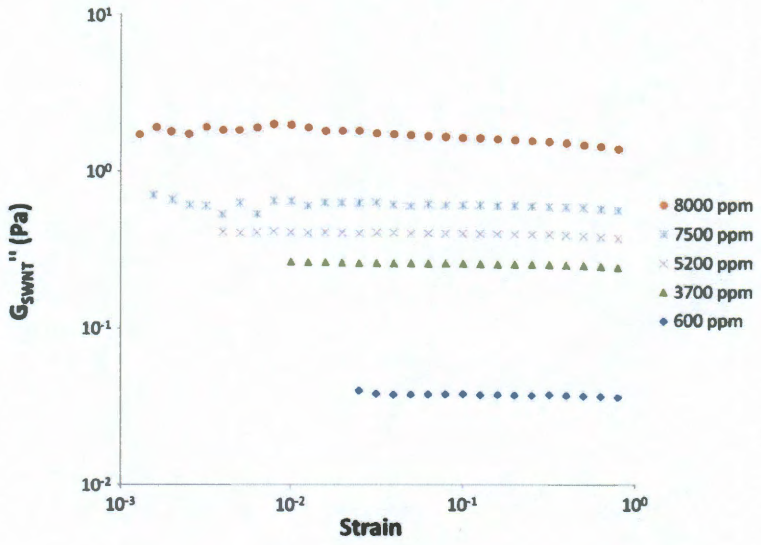

(a)

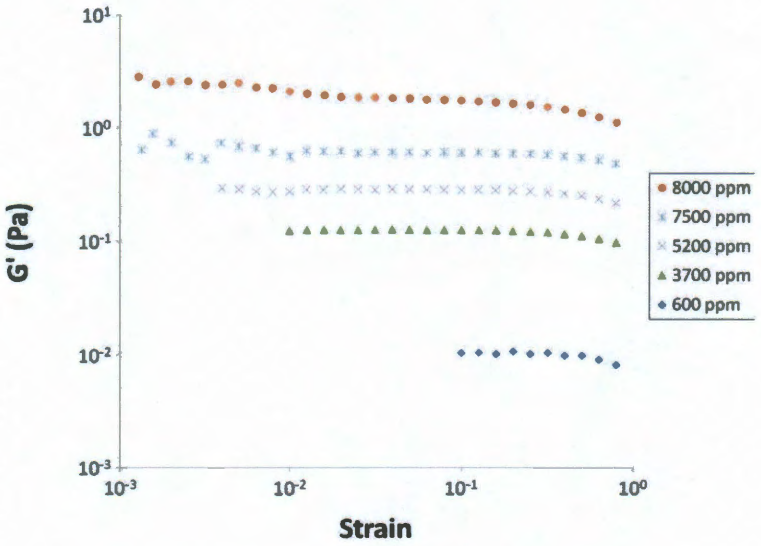

(b)

Figure 4.1: (a) G''_{SWNT} and (b) G' measured via strain sweep tests for SWNTs in ClHSO_3 at concentrations between 600 ppm and 8000 ppm, at a frequency $\omega = 3.14$ rad/s. Data points for which the torque due to stress from the fluid was less than 0.1 μNm have been omitted.

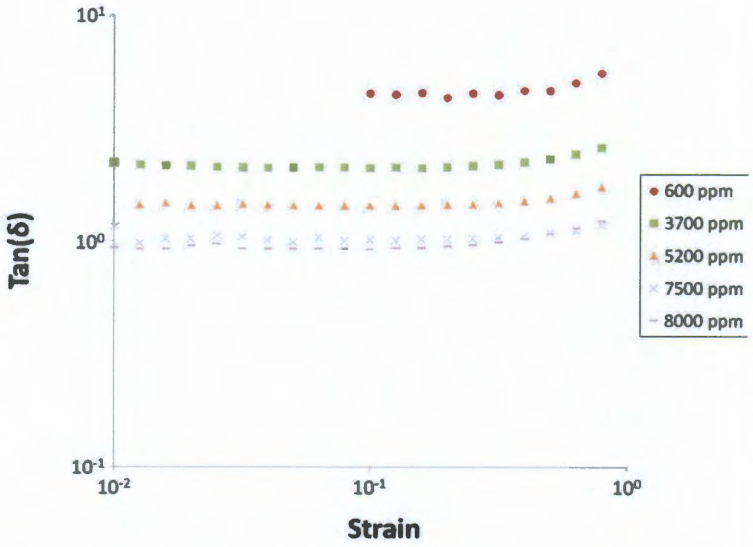

Figure 4.2: Loss modulus tan(δ) vs. strain, calculated from the results shown in Figure 4.1 for SWNTs in $ClHSO_3$ at concentrations between 600 ppm and 8000 ppm. Lower values of tan(δ) indicate a greater magnitude of elastic stress relative to that of viscous stress.

ppm, followed by a steep drop betwen 3700 ppm and 800 ppm to a second plateau value at 6%. At concentrations higher than 3.6 vol% there is a gradual decrease to 2%. In 102% H_2SO_4, γ_c is apparently greater than 100% strain at a concentration of 50 ppm (this was the highest strain value tested), and decreases to 9.7% at 240 ppm. γ_c then plateaus briefly at 2.5% between 430 ppm and 1200 ppm before rapidly decreasing to a broad plateau with a value of approximately 0.19% at concentrations above 3200 ppm. At all concentrations at which a comparison can be made, γ_c of 102% H_2SO_4 solutions is much lower than that measured in $ClHSO_3$ solutions. The conclusions that can be drawn from Figure 4.3 are that SWNT structure generally becomes more sensitive to strain as concentration increases, and that the structures formed in 102% H_2SO_4 are much more sensitive to strain than those found in $ClHSO_3$ at equivalent concentrations. The sharp drops in γ_c at 8000 ppm in $ClHSO_3$ and at 3600 ppm in 102% H_2SO_4 are evidence of percolation in the solutions, and will be discussed in further detail in § 4.1.3.

An examination of the trend in tan(δ) with concentration is included in the discussion of frequency sweep test results that follows. Based on the results of strain sweep experiments depicted in Figure 4.1, frequency sweep experiments were performed on these solutions using a

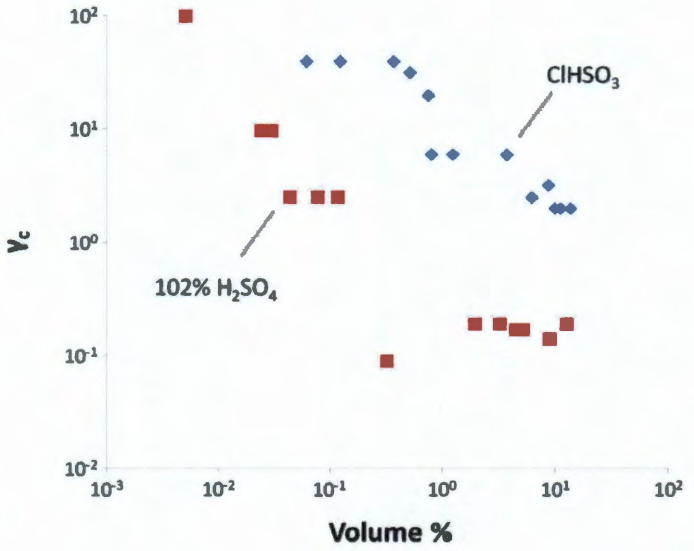

Figure 4.3: Critical strain γ_c vs. concentration, derived from strain sweep measurements on SWNT solutions in both $ClHSO_3$ and 102% H_2SO_4. Data included in the plot comes from the current study as well as past studies on SWNTs in superacids. For all concentrations at which a comparison can be made, γ_c is greater in $ClHSO_3$ than in 102% H_2SO_4, indicating a more extensively connected network which is disrupted by smaller strains.

strain amplitude of 10%.

Figure 4.4 plots the values of elastic modulus $G'(\omega)$ and $G''_{SWNT}(\omega)$ for the aforementioned solutions of SWNTs in $ClHSO_3$. At lower concentrations, the data is truncated at higher frequencies because of interference from the inertial torque of the rotor. Two trends can be easily observed in Figure 4.4. First and most obviously, the values of both moduli increase with increased SWNT loading. Second, as discussed above, and as observed also from strain sweep measurements, the relative magnitude of the viscous and elastic stress contribution from the SWNTs changes, with elastic stress increasing in relative strength as SWNT concentration increases. For low concentration solutions, G''_{SWNT} is greater than G' at all frequencies. For concentrations of 7500 and 800 ppm there is a critical frequency ω_c at which G' crosses G''_{SWNT}, becoming dominant at higher frequencies. For strains applied over times longer than $1/\omega_c$ the elastic response dominates, whereas faster motion involves more viscous loss of energy; as the concentration of SWNTs increases and a more extensive network is formed, elastic effects are important at shorter time scales, and ω_c increases . The trends of G' and G''_{SWNT} with concentration are discussed below in

the context of all the data collected for SWNTs in both $ClHSO_3$ and 102% H_2SO_4 acid.

In general, the frequency dependence of the viscoelastic moduli of polymer solutions is expected to change over a sufficiently large frequency range, because different relaxation mechanisms are probed at different time scales (Morse, 1998). In the case of SWNT/$ClHSO_3$ solutions, the power law scaling of G' and G''_{SWNT} with frequency is consistent across the measured frequency range at each concentration. This indicates that at each concentration, the same relaxation mechanisms determine the stress response across the range of time scales investigated. In order to find the time scales at which the solutions transition from one relaxation mechanism to another, a broader accessible frequency range would be required (i.e., an apparatus with greater torque sensitivity or less sensitivity to problems caused by instrument inertia).

The trend of viscoelastic modulus with concentration can be examined by choosing a given frequency and comparing the modulus values from each solution at that frequency; this provides a comparison of the stress response of the various solutions in response to a strain applied on the same time scale. Modulus values for SWNTs in $ClHSO_3$ measured in this study and in past experiments at higher concentrations are plotted in Figure 4.5 and Figure 4.6 for two different frequency values, 0.1 rad/s and 2.5 rad/s. The trends in the data are similar at both frequencies. Modulus values increase gradually at low concentrations and high concentrations, with a more dramatic increase in the range between 3000 ppm and 1.2 vol%. The fact that the slopes change in this way is in indication that the contribution of each individual SWNT to the viscoelastic stress varies with concentration, i.e., each SWNT contributes a greater amount to total stress at intermediate concentrations than at low or high concentrations; this in turn reflects the fact that the microstructure of the solution varies with concentration, from isotropic to biphasic to liquid crystalline, resulting in different mechanisms of entanglement and interaction.

G' and G''_{SWNT} measured at 2.5 rad/s in $ClHSO_3$ are plotted again in Figure 4.7, this time with the addition of data acquired from 102% H_2SO_4 solutions. This frequency was chosen for the comparison because it is the lowest frequency at which measurements of 30 ppm SWNTs in 102% H_2SO_4 performed in Davis (2006) produced a measurable torque. This data extends to lower concentrations than could be measured in $ClHSO_3$ because the data was acquired on a

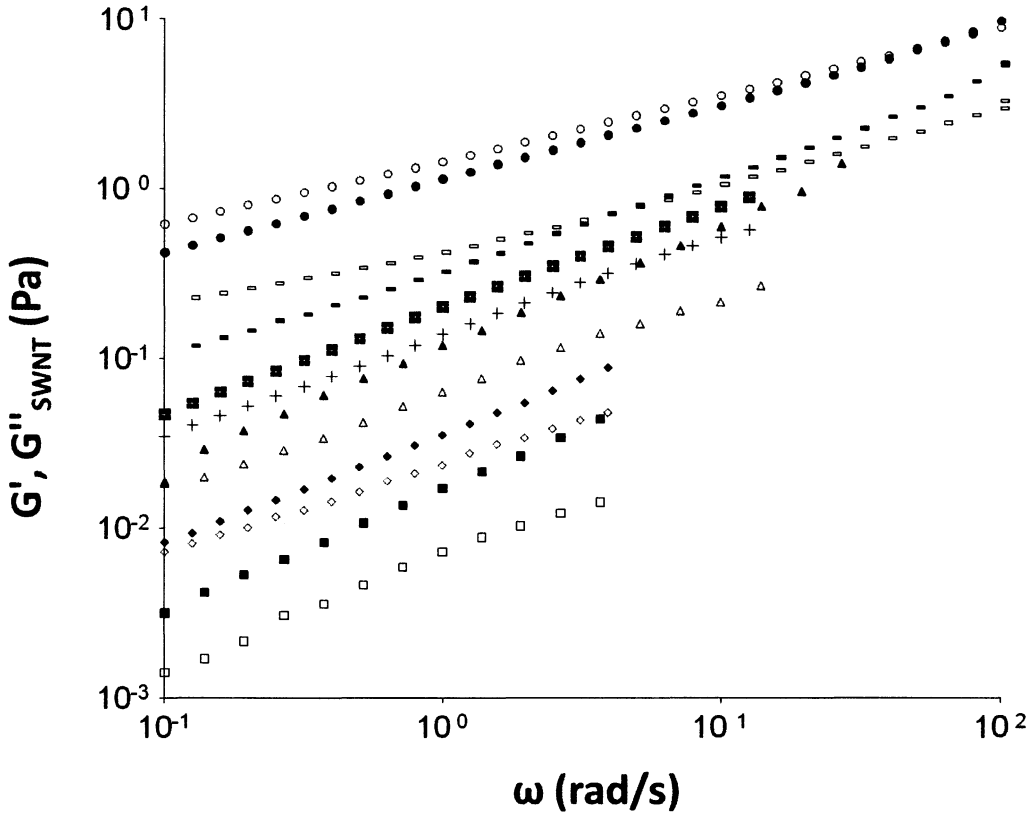

Figure 4.4: Viscoelastic moduli measured as a function of frequency for SWNT solutions in $ClHSO_3$. Filled symbols represent the viscous modulus G''_{SWNT} and open symbols represent the elastic modulus G'. Solution concentrations measured are 600 ppm (squares), 1200 ppm (diamonds), 3600 ppm (triangles), 5200 ppm (crosses), 7500 ppm (rectangles), and 8000 ppm (circles). G''_{SWNT} dominates in low concentration solutions. At 7500 ppm and 8000 ppm G' and G''_{SWNT} cross at a certain frequency ω_c; the value of this crossover frequency increases with concentration, indicating that as SWNT concentration increases, elastic stress is dominant over a broader range of time scales.

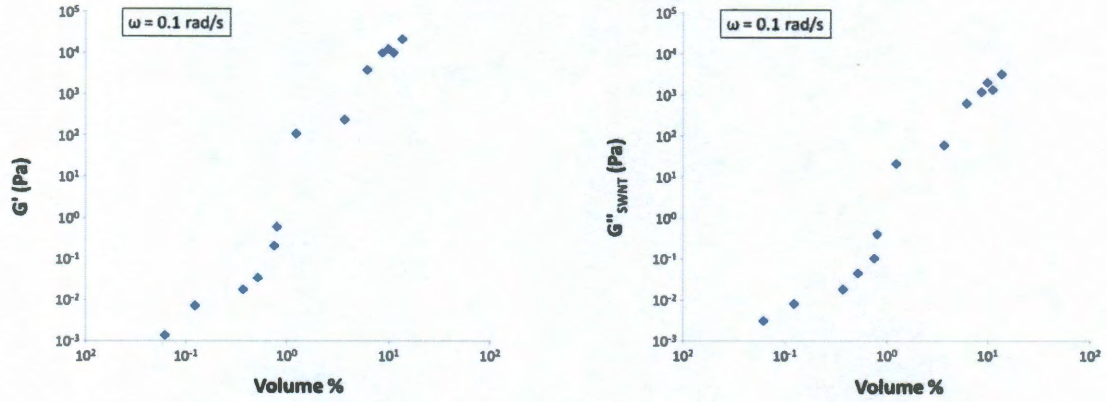

Figure 4.5: (a) G' and (b) G''_{SWNT} measured for SWNTs in $ClHSO_3$ over a concentration range spanning from 600 ppm to 12 vol%. Measurements were conducted with an applied frequency $\omega = 0.1$ rad/s. Both moduli increase with concentration, with a range of rapid increase occurring between 5200 ppm and 1.2 vol%.

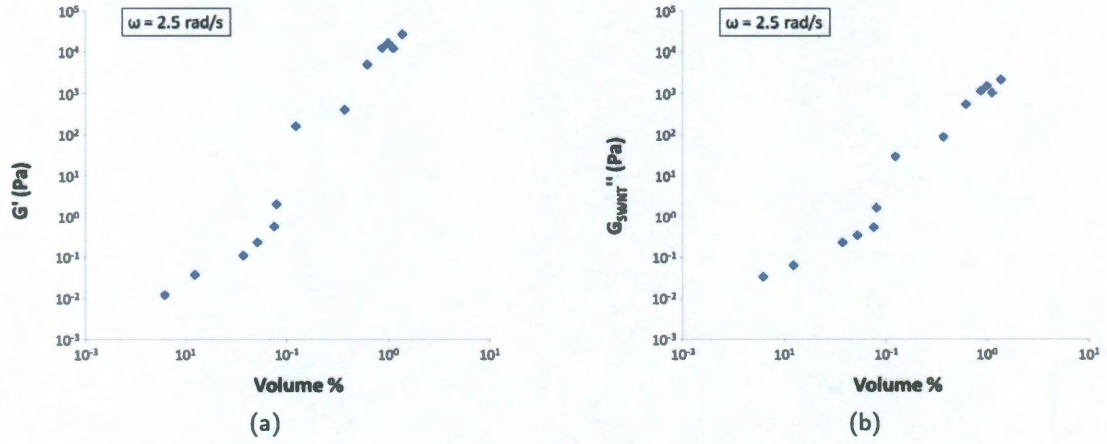

Figure 4.6: (a) G' and (b) G''_{SWNT} measured for SWNTs in $ClHSO_3$ over a concentration range spanning from 600 ppm to 12 vol%. Measurements were conducted with an applied frequency $\omega = 2.5$ rad/s. the trends in the moduli at this frequency are very similar to those observed at $\omega = 0.1$ rad/s, which is a consequence of the fact that the trends of G' and G''_{SWNT} for each concentration do not change within this frequency range.

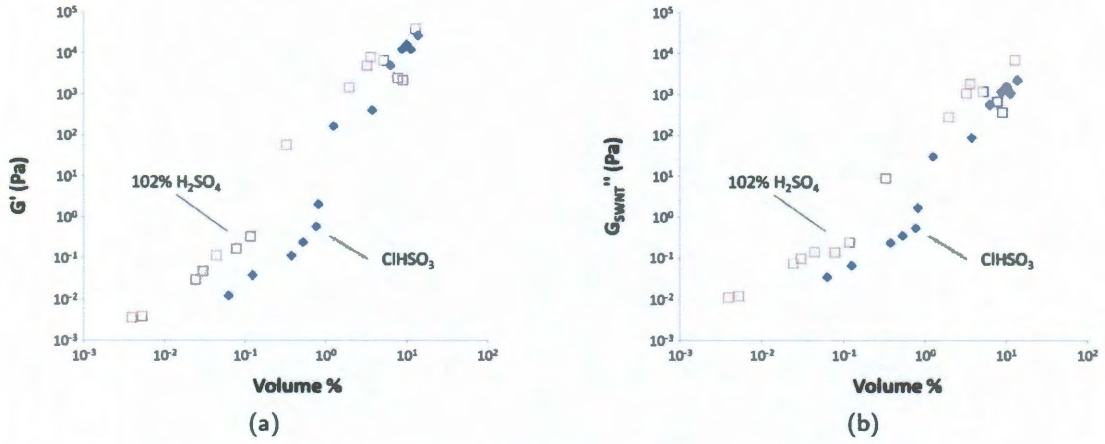

Figure 4.7: (a) G' and (b) G''_{SWNT} measured for SWNTs in both $ClHSO_3$ (closed diamonds) and 102% H_2SO_4 (open squares). The general features of the curves are the same in both acids: there is a gradual increase in modulus values at low concentrations and at high concentrations, with a more rapid increase at intermediate concentrations. In 102% H_2SO_4 the most rapid increase occurs between 1200 and 3200 ppm, in with G' increasing by roughly two orders of magnitude. In $ClHSO_3$ an even more rapid increase occurs between 7500 ppm and 1200 ppm, with G' changing by a factor of ~300. The monotonic behavior of G' and G''_{SWNT} in both acids at the highest measured concentrations is a feature of liquid crystalline solutions that has been discussed in Banzola (2008) and Davis (2006).

different rheometer - a strain controlled ARES rheometer, in which the torque transducer measuring the fluid reponse is coupled to the stationary part of the geometry, and which therefore does not suffer from rotor torque interference. This rheometer has not been used for the current study because it has not been modified for work in an environment as thoroughly moisture-free as is required for safe work with $ClHSO_3$; tests on 102% H_2SO_4 were possible with a smaller enclosed environment encasing the testing geometry and flushed with inert gas, with exposure to moisture only during sample loading. In Figure 4.7 the shape of the data curve for 102% H_2SO_4 solutions is similar to that of $ClHSO_3$ solutions, with a dramatic increase in both G' and G''_{SWNT} between 1200 ppm and 3200 ppm. At the highest concentrations measured, both curves experience a local maximum and minimum; this behavior has been described by Banzola (2008) and Davis (2006) and will not be discussed in detail here.

The viscoelastic properties measured at low concentrations can provide insight into the behavior of SWNT solutions which are isotropic (in $ClHSO_3$) or nearly isotropic (in 102% H_2SO_4). The viscoelastic properties of rigid rod solutions have been theoretically described by Doi & Ed-

wards, Odijk, and others. HiPco SWNTs have a high bending stiffness, giving them a persistence length in the range of 20-80 μm, many times their actual length (Fakhri *et al.*, 2009). For this reason, a rigid rod model is expected to provide a good description of SWNTs. A comparison of low concentration viscoelastic data to predictions derived from rigid rod models is made in § 4.1.4.

We now return to the change in $\tan(\delta)$ with concentration that was previously noted in the results of strain sweep measurements. The increase in the relative magnitude of elastic modulus G' over viscous modulus G''_{SWNT} with increasing concentration is also clear from a comparison of Figure 4.7 (a) and (b). Figure 4.8 depicts the loss modulus $\tan(\delta)$ calculated from the data that is depicted in Figure 4.7, spanning all measured concentrations in both 102% H_2SO_4 and $ClHSO_3$. The dominant modulus in 102% H_2SO_4 solutions changes from G''_{SWNT} to G' around a concentration of 440 ppm, whereas this transition does not occur in $ClHSO_3$ until a concentration of 7500 ppm. In both acids, this transition occurs at concentrations above the biphasic transition, and reflects the increase in elasticity brought about by the creation of liquid crystalline domains.

There is a third significant trend in viscoelastic properties with concentration, which is not immediately apparent in Figure 4.4 but which becomes clear when the data is compared to measurements on higher concentration solutions; this is a change in the frequency dependence of the viscous and elastic moduli, reflecting that fact that the relaxation mechanisms probed by the experiment change with concentration. At higher concentrations, the frequency dependence of $G'(\omega)$ and $G''_{SWNT}(\omega)$ decrease. This effect will also be discussed in detail below.

The dependence of the viscoelastic moduli on frequency can be approximately determined by a power law fit to the curves of $G'(\omega)$ and $G''_{SWNT}(\omega)$, with the assumption that the dependence at a given frequency can be approximated by:

$$G'(\omega) \sim \omega^j \tag{4.1}$$

$$G''_{SWNT}(\omega) \sim \omega^k \tag{4.2}$$

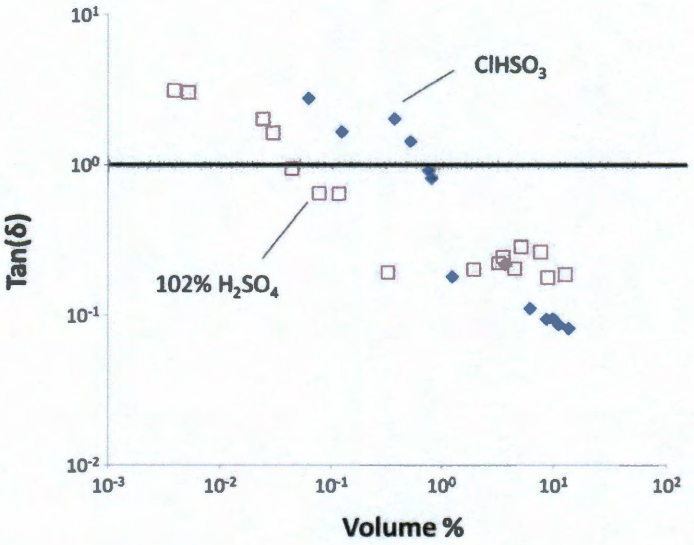

Figure 4.8: Loss modulus tan(δ) calculated from viscoelasticity data measured at a frequency $\omega = 2.5$ rad/s for SWNT solutions in both 102% H_2SO_4 and $ClHSO_3$. $G''_{SWNT} > G'$ if tan(δ) > 1, and the reverse is true if tan(δ) < 1. A horizontal line marks tan(δ) $= 1$, which represents crossover between dominant G''_{SWNT} and G'. In $ClHSO_3$ this transition coincides with the sharp increase in modulus values at 7500 ppm and occurs after the onset of the biphasic regime. In 102% H_2SO_4 the transition also occurs in the biphasic regime, but it occurs before the corresponding sharp increase in modulus values that occurs in that acid at 1200 ppm - this increase is nevertheless accompanied by a further significant drop in tand(δ).

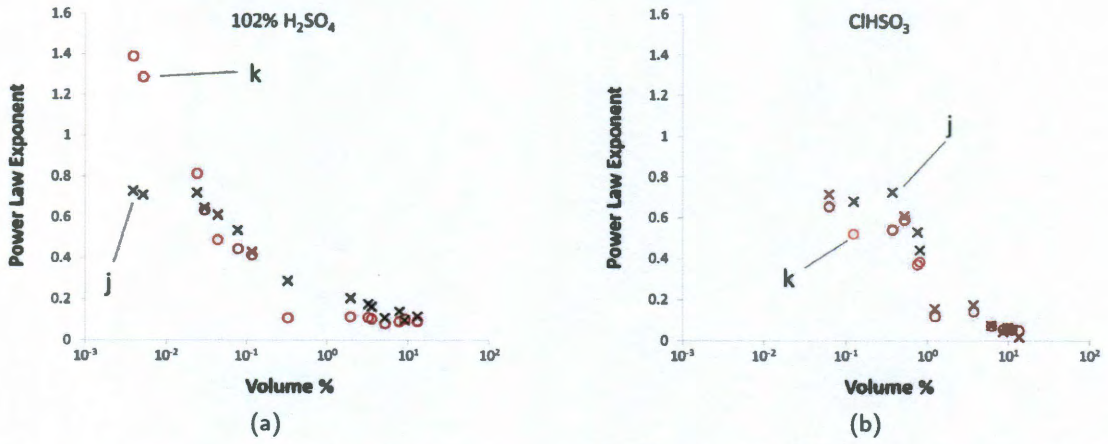

Figure 4.9: Plot depicting how the power law exponents j and k, which are derived from power law fits of G' and G''_{SWNT} vs. ω, change with concentration for SWNT solutions in (a) 102% H_2SO_4 and (b) $ClHSO_3$. At high concentrations in both acids, both parameters reach a low-value plateau, indicating that the solutions have a solid-like viscoelastic stress response that is independent of frequency. The transition to this low-value plateau takes place rapidly in $ClHSO_3$ between 7500 ppm and 1.2 vol%; in 102% H_2SO_4 the transition occurs more gradually.

The change in frequency dependence of G' and G''_{SWNT} with SWNT concentration can therefore be evaluated by plotting j and k vs. SWNT concentration. This is shown in Figure 4.9 using j and k fit parameters from measurements on SWNT solutions in both $ClHSO_3$ and 102% H_2SO_4.

In both acids, there is a decrease in frequency dependence of viscoelastic properties with increasing SWNT concentration, with each curve reaching a plateau at higher concentrations in which frequency dependence is negligible, at least within the range of frequencies tested. In $ClHSO_3$, the decrease in j and k is rapid, occurring over the span of a half decade in concentration between 3700 ppm and 1.2 vol%; in 102% H_2SO_4, however, the loss of frequency dependence occurs more gradually, with a drop spanning a full decade for j, and even longer for k. This more gradual decrease in j and k is explained in § 4.1.3 in terms of the development of the spaghetti liquid crystalline domains.

4.1.3 Percolation

Between 0.117 and 0.324 vol% in 102% H_2SO_4, and between 0.75 and 1.23 vol% in $ClHSO_3$, several phenomena indicate the onset of a percolated structure; first, there is a significant increase

in G' at these concentrations (Figure 4.7). Second, it is within this concentration range that the elastic modulus in $ClHSO_3$ solutions begins to dominate the viscous modulus, indicated by the transition to $\tan(\delta) < 1$ in Figure 4.2. In 102% H_2SO_4 this transition occurs at a lower concentration, as described above, so $\tan(\delta)$ is already less than 1 at a SWNT concentration of 1200 ppm; nevertheless there is a steep drop in $\tan(\delta)$ between 1200 ppm and 3200 ppm, indicating a further significant increase in the dominance of the elastic modulus, followed by a low value plateau at all higher concentrations. Third, elastic structure formation is evident from the power law dependence of the viscoelastic moduli on frequency, $G'(\omega) \sim \omega^j$ and $G''_{SWNT}(\omega) \sim \omega^k$. Above the concentrations in question in either acid the frequency dependence of both moduli becomes negligible, indicating a transition to a structure with solid-like elastic behavior (Figure 4.9). Finally, the drops in γ_c that are observed starting at 7500 ppm in $ClHSO_3$ solutions and at 1700 ppm in 102% H_2SO_4 solutions reflect the creation of a tightly connected network structure, which can be easily disrupted by small strains.

At concentrations just above the percolation threshold the network elasticity $G'(\omega)$ is expected to exhibit a low frequency plateau with magnitude $G_0 \sim (\phi - \phi^*)^\nu$, where ϕ^* is the percolation threshold concentration. Power law fits of G_0 vs. $(\phi - \phi^*)^\nu$ are shown in Figure 4.10 (a) and (b) for SWNTs in 102% H_2SO_4 and $ClHSO_3$, respectively. Here G_0 is taken to be the value of G' measured at frequency $\omega = 0.1$ rad/s, the lowest frequency measured in these experiments; given the low dependence of G' on frequency at the concentrations being considered, this is a reliable value for the elastic plateau modulus. The values of ϕ^* that provide the best power law fits are 0.00113 (0.113 vol%) in 102% H_2SO_4 and 0.0072 (0.72 vol%) in $ClHSO_3$. The power law exponent in the case of $ClHSO_3$ is $\nu_c = 1.92$, and the exponent in the case of 102% H_2SO_4 is $\nu_s = 1.54$. The percolation threshold is reached in $ClHSO_3$ very shortly after the onset of the biphasic regime (differing by around a factor of 2); in 102% H_2SO_4, on the other hand, percolation occurs at a concentration that is significantly higher than the onset of the biphasic regime (by more than an order of magnitude).

These results can be interpreted in the context of SWNT phase behavior in the following way: in $ClHSO_3$, SWNTs appear to percolate at a concentration very close to the isotropic-biphasic

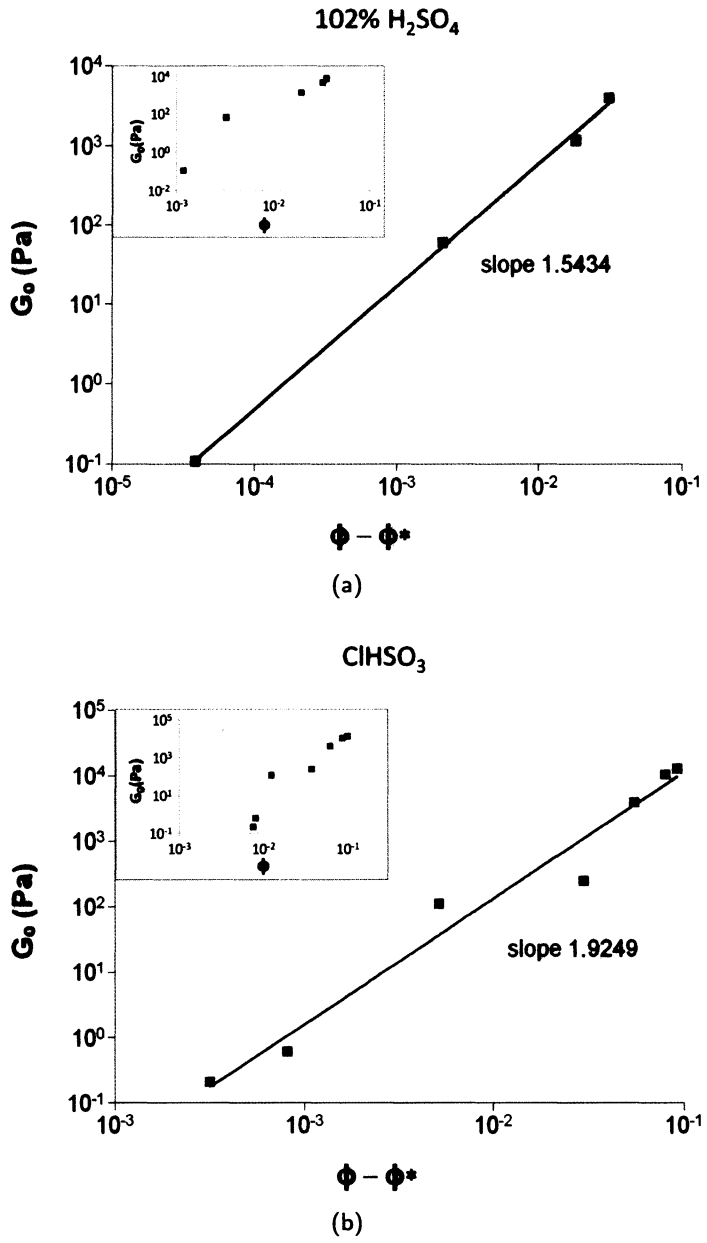

Figure 4.10: Critical power law scaling of elasticity above the percolation concentration in (a) 102% H_2SO_4 and (b) $ClHSO_3$. Low frequency elastic modulus $G_0 = G'(0.1)$ is plotted vs. reduced volume fraction $(\phi - \phi^*)$, where ϕ^* is the percolation threshold concentration. Insets show the data plotted vs. non-reduced volume fraction ϕ. By varying ϕ^* to achieve the best power law fit, we determine that $\phi^* = 0.0072$ (0.72 vol%) in $ClHSO_3$ and $\phi^* = 0.000113$ (0.113 vol%) in 102% H_2SO_4. The difference in percolation thresholds arises from the fact that an elastic network froms due to percolation of overlapping spaghetti domains in 102% H_2SO_4, in contrast to jamming of a primarily homogeneous SWNT glass in $ClHSO_3$. The percolation exponents are $\nu_c = 1.9$ in $ClHSO_3$, which is similar to that measured for other isotropic rod networks, and $\nu_s = 1.54$ in 102% H_2SO_4, which indicates that in weaker acid new SWNTs added to the solution have a weaker effect on the total network elasticity, i.e., that fewer new elastic connections are formed by each SWNT.

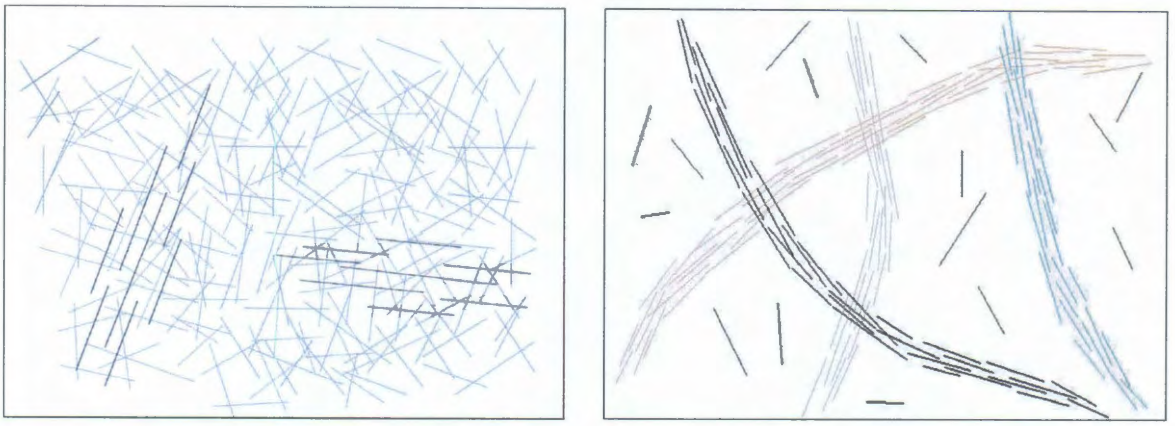

Figure 4.11: Illustration of the proposed microstructure of SWNTs in (a) $ClHSO_3$ and (b) 102%H_2SO_4 near their respective percolation thresholds. In $ClHSO_3$, the SWNTs are predominantly isotropic and homeogeneously dispersed, with some liquid crystalline tactoids present; they form a jammed glass network at approximately the same concentration at which excluded volume interactions induce the creation of liquid crystalline domains. In 102% H_2SO_4, increased attraction drives the creation of liquid crystalline domains at much lower concentrations, before the SWNTs percolate. Because many SWNTs are incorporated into highly elongated aligned domains rather than homogeneously dispersed, they are able to form a space-filling connected network at a lower concentration.

transition, at which the majority of SWNTs are in the isotropic phase. To use the classification system proposed by Solomon and Spicer (2010), it appears that the $ClHSO_3$ solutions exhibit behvior similar to a rigid rod glass: The dissolved SWNTs are isotropically and homogeneously dispersed throughout the fluid, and they form a jammed network once the inter-SWNT distance becomes short enough that excluded volume interactions significantly hinder movement. At a slightly lower concentration, excluded volume interactions also become the driving force behind the transition to liquid crystalline ordering. The percolating system in $ClHSO_3$ is therefore a combination of many isotropic SWNTs and a few tactoid liquid crystalline domains (schematically depicted in Figure 4.11)

In contrast, 102% H_2SO_4 solutions do not appear to undergo percolation until well after the transition to a biphasic solution; the formation of the liquid crystalline phase in this acid is driven not only by excluded volume interactions but also by inter-SWNT attraction. The concentration at which percolation does occur is lower than it is in $ClHSO_3$ due to the presence of long, threadlike liquid crystalline domains (spaghetti domains). Because a significant proportion of

the SWNTs are arranged in these long structures rather than spread homogeneously throughout the fluid, a connected network can be formed at concentrations below that at which percolation would otherwise occur (schematically depicted in Figure 4.11 (b)). The transition to solid-like behavior, characterized by higher modulus and lower frequency dependence, is more gradual in 102% H_2SO_4 than it is in $ClHSO_3$. This is indicated by the smaller scaling exponent $\nu_s = 1.54$ and the more gradual loss of frequency dependence depicted in Figure 4.9. The intuitive explanation for this is that as the liquid crystalline phase develops and more spaghetti domains are created, an increasing number of entanglements are formed, creating an elastic network which gradually increases in strength; this is in contrast to a rod glass which is formed rapidly with the addition of the last few rods once the solution is near the jamming point. The observation of this difference is in accord with the prediction of Solomon and Spicer that rod solutions exist with a continuum of behavior between the two extremes of rod gel formation and the sudden jamming of rod glasses. The structure formed in the limiting case of highly attractive rods is a highly inhomogeneous fractal gel, which percolates gradually and at low concentrations. The attractive forces in 102% H_2SO_4 are not strong enough to form a fractal gel, but do create an inhomogeneous domain structure which falls in between a glass and a fractal gel in terms of percolation behavior.

The critical scaling exponent, ν, reveals the way in which the number of elastic network connections scales with concentration. Theoretical calculations of this exponent for a system of percolating rods predict a value of 3.75 for rods which form rigid connections which are unable to rotate, such as crosslinked polymers, and a value of 2.1 for systems in which the contacts serve as points which resist bending, but are free to rotate (Morse, 1999). The contact points between SWNTs in $ClHSO_3$ should show the latter behavior, and the measured exponent of $\nu_c = 1.92$ is in good agreement with this value. Similar values have been reported in other rigid rod systems that form an isotropic network; SWNTs in aqueous solutions stabilized by SDBS have been observed to have an exponent $\nu \approx 2.3$ (Hough *et al.*, 2004), and a value of $\nu = 1.9$ has been measured for weakly attractive PMMA rods which form a jammed rod glass (Shetty *et al.*, 2010).

The lower percolation exponent observed for 102% H_2SO_4 solutions, $\nu_s = 1.55$, indicates

that each SWNT added to the system after percolation contributes less to the system elasticity than is the case in $ClHSO_3$. This provides further evidence for the model described above: if the entanglements that create the elastic network are the points of contact between spaghetti LC domains rather than between individual SWNTs, then the number of SWNTs required to create a new entanglement will be on the order of the number of SWNTs present in a single spaghetti strand. By contrast, in a jammed glass each new SWNT is likely to create new entanglements in the network.

The value of ν_s is also very similar to the exponent of 1.55 found for HiPco SWNTs in unsaturated polyester resin, but the microstructures of the two systems are different; in that system the SWNTs were isotropically dispersed with no liquid crystalline domains present, and the low value of the scaling exponent was attributed to poor dispersion/bundling of the SWNTs (Kayatin, 2008).

An interesting contrast can be drawn between the percolation phenomenon in superacid solutions and that of systems with stronger attractive interations. It has been observed in colloidal systems, soft glasses, and suspensions of MWNTs that $G'(\omega)$ and $G''_{SWNT}(\omega)$ from solutions of different concentrations can be collapsed onto a single pair of curves by a rescaling of both the moduli and the frequency by concentration-dependent factors (Trappe and Weitz, 2000; Cicuta *et al.*, 2003; Hobbie and Fry, 2007). This indicates that the solutions at different concentrations (above the percolation concentration of the system) possess a fractal structure with self-similar microstructure at every concentration. The physical response of such a system on one time scale mimics the response that a more concentrated structure has on a shorter time scale. This feature of fractal networks is useful because it provides a means of extrapolating low concentration/low frequency behavior which may otherwise be experimentally inaccessible.

The MWNT systems that form this kind of fractal network structure are typified by strong attractive interactions between surfactant-wrapped nanotubes. SWNT/superacid solutions, on the other hand, are not expected to form a fractal network because they lack the strong inter-SWNT attraction that would promote such a structure. Rather than adhering to one another, **SWNTs in concentrated superacid solutions are able to flow and rearrange to find thermodynam-**

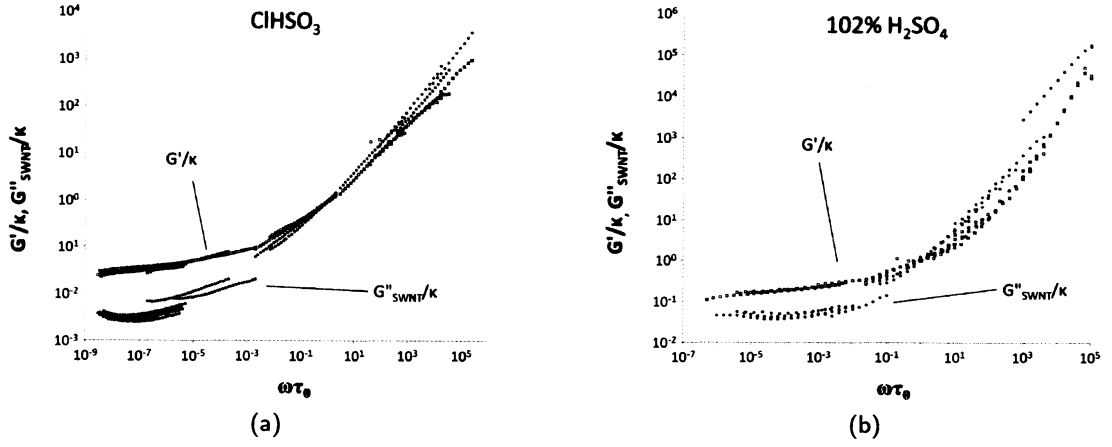

Figure 4.12: Rescaled elastic modulus (open symbols) and viscous modulus (closed symbols) for (a) SWNTs in $ClHSO_3$ and (b) SWNTs in 102% H_2SO_4. Modulus and frequency scaling factors $\kappa(\phi)$ and $\tau(\phi)$ were determined empirically to achieve the best collapse onto a single curve for the G' data. In both cases, the collapse of G''_{SWNT} data onto a single curve using the same scaling factors is not successfull. This illustrates the fact that SWNTs in superacids do not form a fractal gel structure with self-similarity across multiple concentrations; instead, the transition from isotropic to liquid crystalline solution results in the formation of highly dissimilar microstructures as concentration changes.

ically favorable configurations, which is why they are able to form liquid crystals. To illustrate this, a technique similar to that used in the above cases has been employed here to determine whether $G'(\omega)$ and $G''_{SWNT}(\omega)$ for SWNT/acid solutions can be collapsed onto a single master curve.

An attempt has been made to scale the viscoelasticity data for SWNTs in $ClHSO_3$ and 102% H_2SO_4 onto master curves using an empirically determined scaling modulus $\kappa(\phi)$ and time scale $\tau(\phi)$. Both scaling factors were chosen such that G' from all concentrations collapses onto a single master curve; the same factors were then applied to rescale G''_{SWNT} and the results are plotted in Figure 4.12. This scaling is successful between 0.37 and 1.23 vol% in $ClHSO_3$ and between 0.024 and 0.117 vol% in 102% H_2SO_4. Data from concentrations above and below these ranges could not be collapsed onto the same set of master curves, as seen in the deviations and discontinuities in G''_{SWNT}/κ. The moduli can be scaled independently onto smooth master curves, but this produces significant disagreement in the separate scaling factors. The fact that this rescaling method fails to produce smooth master curves over the range of concentrations considered

reflects the changing nature of the SWNT microstructure; as the phase of each solution evolves from isotropic to increasingly liquid crystalline, the geometry of the microstructure changes, and the structure at different concentrations therefore does not possess self-similarity. The concentration regimes in which the data can be collapsed can be thought of as small concentration sindows in which the fundamental geometry of the microstructure changes only slightly. This behavior highlights a fundamental difference between the rheology of SWNT solutions that undergo a liquid crystalline transition and the surfactant-stabilized MWNT solutions investigated by Hobbie and Fry (2007), in which the inter-SWNT attractive potential is strong enough to promote the formation of a fractal network.

4.1.4 Comparison to Theory

This section will focus on the behavior of SWNT solutions in both 102% H_2SO_4 and $ClHSO_3$ at concentrations below the percolation transition and consider this behavior in the context of models that have been developed for the behavior of rigid rod solutions. The model considered here is based on the theory derived by Doi & Edwards for rigid rods, incorporating the modifications made by Marrucci & Grizzuti to take into account length polydispersity and the extension to the theory made by Odijk to account for slight flexibility of the rods (Doi and Edwards, 1986; Marrucci and Gizzuti, 1983; Odijk, 1983) A calculation of viscoelastic properties that assumes a log-normal length distribution for the dissolved SWNTs has been made based on these models. It is shown that for length distributions consistent with past measurements on HiPco SWNT the model fails to coincide with the experimental data, indicating that solutions of SWNTs in superacids deviate in some way from the behavior assumed by this model.

Below the percolation concentrations, these solutions consist either of isotropically dispersed SWNTs (in the case of SWNTs in $ClHSO_3$ below 3000 ppm), or of isotropic SWNTs intermixed with liquid crystalline SWNT domains (in the case of SWNTs in 102% H_2SO_4 and in $ClHSO_3$ above 3000 ppm). The viscoelastic properties of the solutions in both acids have a similar dependence on concentration below these percolation thresholds, as shown in Figure 4.7. G' scales as $\phi^{1.32}$ in $ClHSO_3$ and $\phi^{1.37}$ in 102% H_2SO_4, while G''_{SWNT} scales as $\phi^{1.1}$ and $\phi^{0.93}$ in $ClHSO_3$ and 102%

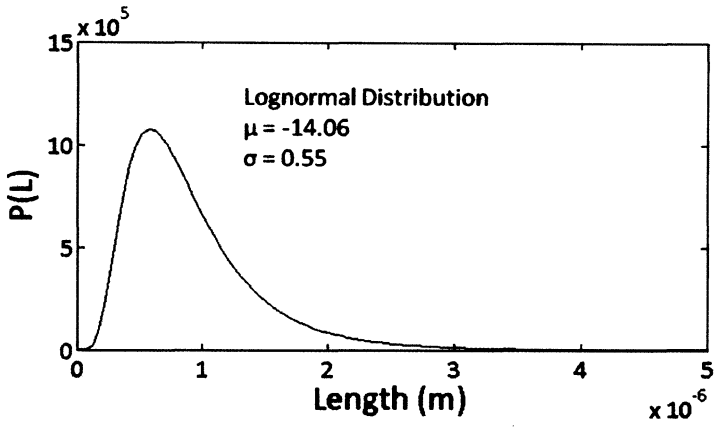

Figure 4.13: Lognormal probability distribution describing the distribution of lengths in a typical HiPco batch. This length distribution results in an average length of $\langle L \rangle = 908$ nm.

H_2SO_4, respectively. This similarity may be an indication that even though some liquid crystalline ordering is present, the behavior of these solutions is predominantly determined by the isotropic SWNTs. It is therefore interesting to compare the viscoelastic properties of solutions in this concentration regime (below 8000 ppm in $ClHSO_3$ and below 1200 ppm in 102% H_2SO_4) to the predictions of rigid rod solution models.

The length distribution of HiPco SWNTs has been measured in the past both by AFM and by rheological measurements (Carver *et al.*, 2005; Parra-Vasquez, 2009). Typically, it can be described by a lognormal length distribution with a peak in the range of a few hundred nanometers. As a starting point for the calculations that follow it is assumed that the SWNTs have a length distribution that is described by a lognormal distribution with $\mu = -14.06$ and $\sigma = 0.55$. This distribution has an average length of 908 nm, in agreement with the results of (Carver *et al.*, 2005) for the standard HiPco reactor condition of 52 mTorr catalyst pressure. The length distribution is plotted in Figure 4.13. A small portion of the SWNTs in the distribution have lengths of a few μm, and the probability distribution becomes negligible at lengths higher than 3 μm. SWNT diameter is assumed to be 1 nm in the following calculations (average for HiPco is 1.09 nm).

4.1.4.1 Suitability of the assumption that orientational stress is dominant

Morse (1998) has described the time scales on which various physical effects will dominate the

viscoelastic behavior of rigid rod solutions. Stress resulting from curvature of rods is expected to dominate on time scales shorter than

$$\tau_{\text{rep}} = \frac{\zeta L^3}{\pi^2 k_B T} \tag{4.3}$$

which represents the time required for a rod to move a distance equal to its own length along its axis, reptating out of caging entanglements. Here,

$$\zeta \simeq \frac{4\pi\eta_s}{\ln\left(\frac{1}{d(\nu L)^{0.5}}\right)} \tag{4.4}$$

For a SWNT of a given length, orientational stress is dominant on time scales longer than τ_{rep}, therefore orientation should dominate measurements taken at frequencies above $\omega = 1/\tau_{\text{rep}}$. According to (4.3), the shortest SWNT for which curvature effects should appear at a frequency of $\omega = 2.5$ rad/s in a $\sim$ 6000 ppm solution in $ClHSO_3$ is 1.1 μm. The time scale calculated in (4.3) is not an exact prediction, but rather an estimate based on scaling laws; however, from this estimate it can be concluded that for a population of SWNTs in the concentration range of interest, with the length distribution shown in Figure 4.13, subjected to oscillatory shear strain at a frequency of 2.5 rad/s, the majority of the SWNTs will exhibit a stress response dominated by orientation effects, with the longest SWNTs potentially contributing curvature stress as well.

This conclusion is consistent with the observed concentration and frequency scaling of these solutions. For rods within the orientation dominated regime, these scaling behaviors vary depending on the magnitude of the term $\tau_{\text{rot}}\omega$ in (2.7) and (2.8). The frequency dependence of G' is ω^2 for $\tau_{\text{rot}}\omega \ll 1$, and gradually transitions to ω^0 as $\tau_{\text{rot}}\omega$ increases; the frequency dependence of G''_{SWNT} should be ω^1, at low frequencies, becoming slightly lower at intermediate values of $\tau_{\text{rot}}\omega \sim 1$ for which the first term in (2.8) deviates from linear scaling itself before becoming negligible, then returning again to a scaling of ω^1. The concentration dependence of G' for semidilute solutions transitions from ϕ^5 to ϕ^1, and the concentration dependence of G''_{SWNT} should be ϕ^3. At higher concentrations, in which the rotational relaxation transitions to that described by Odijk, both moduli should scale linearly with ϕ On the other hand, in the curvature

dominated regime G' should maintain a plateau value independent of frequency and varying with concentration as $\phi^{1.4}$, while G''_{SWNT} should be vary linearly with frequency and concentration (Morse, 1998).

In SWNT/acid solutions at the concentrations in question, G' scales with frequency with a power $j \sim 0.6$ (see Figure 4.9), and scales with concentration with a power between 1.3 and 1.4. G''_{SWNT} also has a frequency dependence of $k \sim 0.6$ and concentration dependence that is approximately linear (having a power law scaling of 1.1 in $ClHSO_3$ and 0.93 in 102% H_2SO_4). This concentration dependence would be consistent with a highly entangled system dominated by orientational stress, with SWNTs possessing a concentration-independent relaxation time as described by Odijk; it would also be consistent with a systems dominated by curvature stress. On the other hand, if curvature stress was a dominant factor, the frequency dependence of G' would be closer to ω^0. It is therefore a reasonable assumption that the viscoelastic stress in these solutions is due to orientational stress, and can be described by (2.7) and (2.8). This assumption should be questioned if the calculated viscoelastic moduli under-predict the measured viscoelastic moduli of the solutions; as we shall see, this is not the case.

One consequence of the orientation stress model provides a simple test for its accuracy in describing the SWNT/acid solution measurements; for a system described by these equations, the viscous modulus will always be greater than the elastic modulus, and as a consequence the loss modulus $\tan(\delta)$ will always be greater than 1. As depicted in Figure 4.8, the experimentally determined $\tan(\delta)$ becomes less than 1 at 430 ppm for SWNTs in 102% H_2SO_4 and at 7500 ppm for SWNTs in $ClHSO_3$. As was noted in § 4.1.3, 7500 ppm corresponds closely to the percolation transition in $ClHSO_3$ and it is also above the biphasic transition in $ClHSO_3$. In 102% H_2SO_4 , 430 ppm is well below the apparent percolation transition, but it is nevertheless above the biphasic transition concentration. We see therefore that the rod solution model cannot be applied to solutions above 7500 ppm in $ClHSO_3$ or 430 ppm in 102% H_2SO_4, most likely because of the **development of significant liquid crystalline ordering in both cases. At the four lowest concentrations** in each acid $\tan(\delta)$ is greater than 1, so the model might apply for these concentrations.

4.1.4.2 Description of the model

In order to compare the low concentration viscoelasticity data to the rod solution model, calculations of $G'(\phi)$ and $G''_{SWNT}(\phi)$ were carried out for a polydisperse rod population having the lognormal length distribution given in Figure 4.13. Based on the assumed diameter of 1 nm, the SWNTs were further assumed to have a persistence length of 50 μm (Fakhri *et al.*, 2009). In order to account for the polydispersity of the sample the length range was broken into discrete populations. For each length population the model was used to calculate the transition concentration from dilute to semidilute behavior as well as the expected rotational relaxation times for the dilute, semidilute, and tightly entangled regimes. Finally, the viscoelastic moduli of the solution were calculated by integrating over the contribution from each length population. The calculations, which are described below, are based on the equations presented in § 2.3.2.

Marrucci & Grizzuti (Marrucci and Gizzuti, 1983) developed an extension of the Doi & Edwards theory for rigid rods to polydisperse length population in which the semidilute transition concentration is determined separately for each length population. Below a certain concentration all of the SWNTs behave as dilute rods; at any given concentration above this, the shortest SWNTs are still able to rotate freely and therefore behave as dilute rods, whereas the longer SWNTs have their rotational motion hindered by others and adopt semidilute behavior. In addition, their theory considers the fact that if a test rod is confined to a virtual tube by the presence of other rods, it can leave that tube either through reptation along its own length or by the reptation of the confining rods out of their positions. The longer the caged rod is compared to the confining rods, the greater the chance that the confining rods will move out of the way before the long rod completes a reptation; this leads to a decrease in the relaxation time of longer rods.

The number of SWNTs expected to intersect a cylinder of radius r around a test SWNT of length L in an isotropic solution is

$$N(r) = \frac{\nu \pi r L}{2} \int P(L')L' \mathrm{d}L' \tag{4.5}$$

This represents a calculation of the number of rods of each length L' which are expected to inter-

sect the virtual cylinder, integrated over all lengths present in the distribution. ν is the number concentration of SWNT and $P(L')$ represents the length distribution; the factor of $\frac{1}{4}$ arises from a consideration of random SWNT orientation. The number concentration $\nu_{\text{semi}}(L)$ yielding the transition to semidilute behavior and the corresponding volume concentration $\phi_{\text{semi}}(L)$ are determined by finding the concentration at which $N(L)$ is equal to the numericall factor α; this empirical numerical factor represents the number of other SWNTs that must pass within possible contact distance of the SWNT in question in order to hinder its rotation. As mentioned in § 2.3.2, α has been found to be approximately 30 - 40 for other rod systems (Larson, 1999; Teraoka and Hayakawa, 1989). For this model the value $\alpha = 30$ has been used.

The rotational relaxation time for SWNTs of length L at concentrations below $\phi_{\text{semi}}(L)$ was calculated using the equation

$$\tau_{\text{rot}} = \frac{\zeta_{\perp} L^3}{72 k_B T} \tag{4.6}$$

Here, $\zeta_{\perp}$ represents the resistence to rotation due to friction from the solvent,

$$\zeta_{\perp} = 4\pi\eta_s \epsilon f(\epsilon) \tag{4.7}$$

in which

$$\epsilon = \frac{1}{\ln(L/d)} \tag{4.8}$$

$$f(\epsilon) = \frac{1 + 0.64\epsilon}{1 - 1.5\epsilon} + 1.659\epsilon \tag{4.9}$$

with d being the diameter of the SWNT.

SWNTs of length L at concentrations higher than $\phi_{\text{semi}}(L)$ were treated as if they were confined to a reptation tube of radius $a(\nu, L)$ such that $N(a) = \alpha$. The rotational relaxation time for these SWNTs was calculated based on the approach of Marrucci & Grizzuti in order to ac-

count for the possibility of shorter rods in the confining tube relaxing themselves and easing the confinement:

$$\tau_{\text{rot}} = \frac{\zeta_\perp}{72 k_B T}\left(\frac{L}{a}\right)^2 \left[\frac{\int_0^L P(L')L'^4 \mathrm{d}L' + L^3 \int_L^\infty P(L')L' \mathrm{d}L'}{\int_0^\infty P(L')L' \mathrm{d}L'}\right] \tag{4.10}$$

Here, the first term in brackets represents faster relaxation due to confinement by rods shorter than L and the second term represents relaxation due to normal reptation, each weighted by the probability that any given confining rod has length L'.

In order to account for flexibility of the rods, the rotational relaxation time was calculated in yet another way for SWNTs confined on the short length scales described by Odijk (Odijk, 1983). This was done by setting the following upper limit on the rotational relaxation time for each length bin:

$$\tau_{\text{rot}} = \frac{\zeta_\parallel L_p L^2}{6 k_B T} = \frac{\zeta_\perp L_p L^2}{12 k_B T} \tag{4.11}$$

This represents the fact that once the confinement of a rod by its neighbors reaches a certain point, the radius of the virtual reptation tube to which the rod is confined becomes comparable to the length scale of slight deflections in the tube backbone arising from it's natural flexibility. In this case, the deflection at the ends of the rod provide a slight re-orientation as the rod moves along its axis. The degree of this re-orientation depends only on the flexibility of the rod as measured by its persistence lenth L_p, and thus the rod is able to relax in the time given by (4.11) regardless of the amount of confinement.

Once the rotational relaxation time of SWNTs in each length population has been calculated, the viscoelastic moduli due to orientational entropy were calculated fopr each length population using equations (2.7) and (2.8), and the total viscoelastic contribution of the SWNTs was calculated by integrating over the contribution from all length populations.

4.1.4.3 Comparison of the model with experimental data

There were several motivations behind this comparison: first, to see if there is indeed any agreement between the model predictions and the experimental results; second, to determine whether the effects of flexibility on reptation as described by Odijk (1983) are important or unimportant in the behavior of rod solutions below percolation; finally, assuming good agreement was found in the case of $ClHSO_3$ solutions, to determine whether or not the attractive interactions between SWNTs in 102% H_2SO_4 solutions results in greater divergence from the model, which assumes an athermal solvent.

First, we consider a model that does not take flexibility into account, and therefore ignores the lower limit on SWNT relaxation time providd by (4.11). Figure 4.14 compares the viscous and elastic moduli calculated with this model for SWNTs in $ClHSO_3$ at a frequency of 2.5 rad/s to the experimentally measured values. The length distribution used for this calculation is the lognormal distribution shown in Figure 4.13. It is obvious from this comparison that the experimental values are greatly at odds with the predictions of the model. The calculated values are many times higher than the measured values; in addition, the relative magnitudes of G' and G''_{SWNT} and the scaling of G''_{SWNT} with ϕ are predicted incorrectly.

The incorporation of Odijk's theory into the model to account for SWNT flexibility results in a marked change in the scaling of G''_{SWNT} with ϕ at higher concentrations, as all but the shortest SWNTs enter the tightly entangled regime in which the concentration dependence of rotational relaxation time vanishes (see (4.11)). The scaling of G' with ϕ is not significantly effected since in this concentration range the calculated value of $\tau_{rot}\omega$ for the majority of SWNTs is large enough to remove the dependence of G' on τ_{rot} entirely. The concentration dependence of the calculated moduli is thus closer to that which was measured; however, as shown in Figure 4.15, the magnitudes of G' and G''_{SWNT} predicted by the model are still several orders of magnitude higher than the measured viscoelastic moduli.

The discrepancy between the model predictions and experimental data is obviously significant; there are a few possible sources for this discrepancy. One possibility is that the SWNTs are

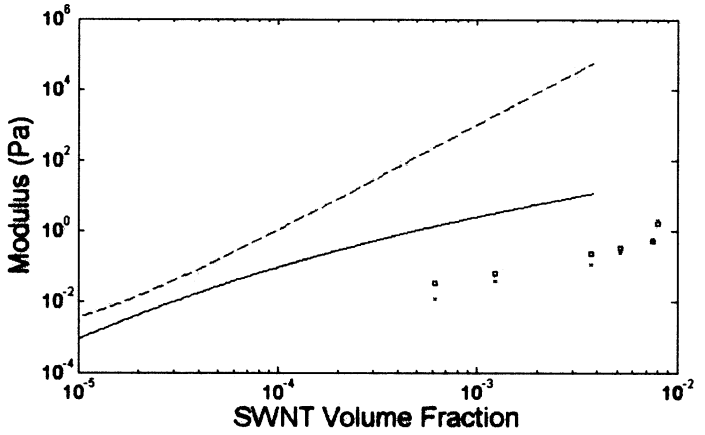

Figure 4.14: G' (solid line) and G''_{SWNT} (dashed line) calculated using a rigid rod solution model for SWNTs in $ClHSO_3$. Also plotted are observed values of G' (crosses) and G''_{SWNT} (squares) determined from dynamic shear rheology. In this case τ_{rot} is calculated using (4.10) for all concentrations above ϕ_{semi}, with no consideration made for flexibility of the SWNTs; as a result, τ_{rot} never becomes independent of concentration and thus G''_{SWNT} continues to scale with concentration as ϕ^3. The calculated values greatly over-predict the modulus values. The SWNT length distribution used in the calculation is given by the lognormal distribution depicted in Figure 4.13.

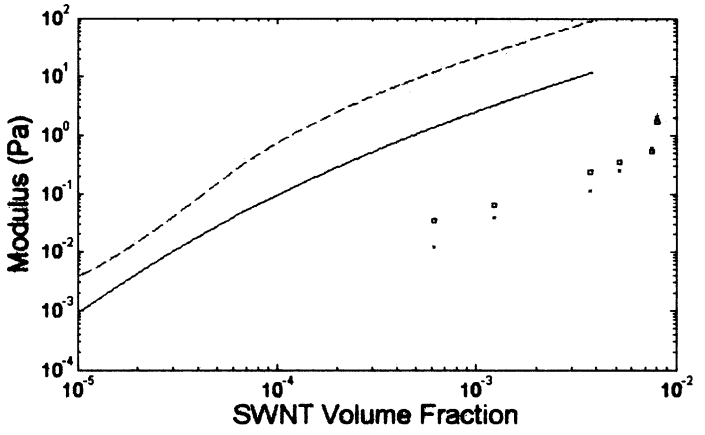

Figure 4.15: G' (solid line) and G''_{SWNT} (dashed line) calculated using a semiflexible rod solution model for SWNTs in $ClHSO_3$, with (4.11) used as an upper bound for the rotational relaxation time in order to account for the effects of flexibility on SWNT movement. In this case the model predicts a scaling of both viscoelastic moduli with ϕ that is in better agreement with that of the experimental data below the biphasic transition at $\sim$ 4000 ppm; however, the predited moduli are still far greater in magnitude than those measured by experiment, as is the ratio of G''_{SWNT} to G'.

significanly shorter than has been assumed. The lognormal length distribution shown in Figure 4.13 was measured by fitting a curve to a histogram of lengths measured in an AFM samples of SWNTs (Carver *et al.*, 2005). This method is imperfect, and may lead to an over-prediction of length due to SWNT bundling on the AFM substrate. Other measurements of Hipco SWNT length distributions conducted through both AFM and measurements of steady shear viscosity have indicated that the average length <L> for Hipco SWNTs may be only a few hundred nanometers (Parra-Vasquez, 2009). Thus, it is worth investigating whether a better agreement can be achieved by assuming a shorter length distribution.

Figure 4.16 compares measured viscoelastic properties for SWNTs in $ClHSO_3$ with those predicted by the model for a SWNT population with <L> = 166 nm. In this case the model predicts dilute behavior up to a volume fraction of 10^{-4}. As concentration rises above this, an increasing number of the SWNT length populations shift to semidilute behavior. In the concentration range spanned here only some of the longest SWNTs are confined tightly enough to adopt the rotational relaxation behavior described by Odijk; as a result, the viscoelastic response predicted by the model is dominated by SWNTs with strongly concentration-dependent rotational relaxation time given by (4.10). Thus although the magnitude of the viscoelastic moduli predicted by the model is in this case much closer to those measured for SWNT solutions, the predicted scaling with concentration is much greater than that of the experimental data. For a distribution with higher <L>, the predicted scaling is weaker due to the onset of concentration-independent relaxation for a greater number of the SWNTs, but the magnitudes of the moduli will increase; for a distribution with shorter <L> the magnitudes will decrease but the scaling with concentration becomes stronger. Error in the SWNT length distribution assumed by the model is therefore insufficient to explain the discrepancies observed here.

Given that the model does not seem to agree with the data for any assumed length distribution, other possible sources for this divergence must be considered. The magnitude and concentration dependence of the experimentally determined moduli indicate that stress in the SWNT microsctructure may be relaxing by some process that is faster than the model predicts, and that this relaxation time is only weakly dependent on concentration; however, it is unclear what the

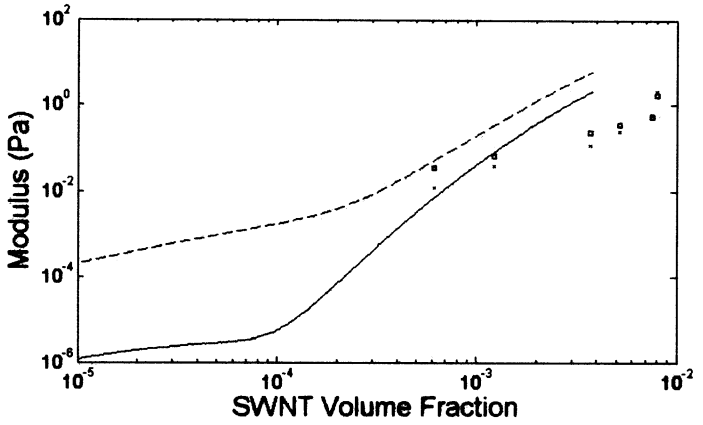

Figure 4.16: G' (solid line) and G''_{SWNT} (dashed line) calculated using a rigid rod solution model for SWNTs in $ClHSO_3$. SWNTs are assumed to have a lognormal distribution of lengths with μ = -14.06 and σ = 0.55, leading to an average length <L> = 166 nm. In this case the viscoelastic moduli arising from the model have magnitudes closer to those found by experiment, but the scaling of these moduli with concentration is predicted to be much stronger than is observed.

mechanism for this relaxation might be. One possible reason for the observed behavior is that the viscoelastic stress in these solutions is indeed dominated by curvature stress after all. This would account for the scaling of the data with concentration; however, the addition of this stress would only lead to an even greater over-prediction of the moduli values unless the length distribution assumed for the SWNTs is very short, with an average length much smaller than the one assumed in Figure 4.16, so that the magnitude of the orientation stress becomes correspondingly smaller.

Another possible explanation that could be considered is that the longest SWNTs may be progressively entering the liquid crystalline phase starting at concentrations lower than 600 ppm in $ClHSO_3$, in spite of evidence pointing to the onset of the biphasic regime at concentrations higher than 3000 ppm. If the longest SWNTs are entering liquid crystalline domains they will be removed from the bulk isotropic phase; this may lead to a negative feedback effect in which the concentration of the isotropic phase itself does not scale linearly with the total SWNT concentration, and in which the length distribution of SWNTs in the isotropic phase is also gradually lowered. Such a mechanism could result in orientation stress with a lower magnitude and weaker concentration dependence. However, this would require the onset of a biphasic phase at con-

centrations one order of magnitude below those at which it has been observed for Hipco SWNTs in $ClHSO_3$.

At the moment the discrepancy between the predictions of a semi-flexible rod model and the viscoelastic properties of SWNTs in superacids is puzzling. Future work attempting to uncover the source of this discrepancy should focus first on the two possibilities explored above. A direct measurement of either the average length or biphasic transition concentration of the Hipco batch used in these experiments may indicate whether one of these theories holds merit.

4.2 Varying Solvent Strength

This section describes the results of dynamic shear measurements made on HiPco SWNTs dissolved in mixtures of $ClHSO_3$ and 102% H_2SO_4. Superacid solvents were created with a range of protonating strength by the inclusion of different proportions of these two acids. The goal of these tests was to study the effect of gradually varying inter-SWNT potential on solution microstructure at a fixed SWNT concentration.

Solutions were mixed at a concentration of 3500 ppm in six different acid solvents: 102% H_2SO_4, $ClHSO_3$, and mixtures of these two acids containing 90%, 70%, 50%, and 30% $ClHSO_3$ by volume. According to the analysis of percolation behavior given above, SWNTs at this concentration in pure $ClHSO_3$ should be isotropic, without any percolated structure, whereas SWNTs in 102% H_2SO_4 should be above their percolation threshold. Light micrographs of samples from these solutions, shown in Figure 4.17 and Figure 4.18, confirm that in the two strongest acids, $ClHSO_3$ and 90% $ClHSO_3$, the solutions are featureless in both normal and polarized light microscopy. In 70% $ClHSO_3$, some birefringent liquid crystalline domains can be detected; similar domains are present in all of the acids weaker than this.

Figure 4.19 (a) plots how the G' and G''_{SWNT} vs. solvent composition; as the degree of SWNT protonation is decreased, both G' and G''_{SWNT} increase, indicating that the structure of the solution varies continuously as SWNT attraction changes. The changes in viscoelastic modulus values in this case may be due to two effects: a change in SWNT structure and interaction as the protonating power of the solvent changes, and a change in solvent viscosity as more viscous

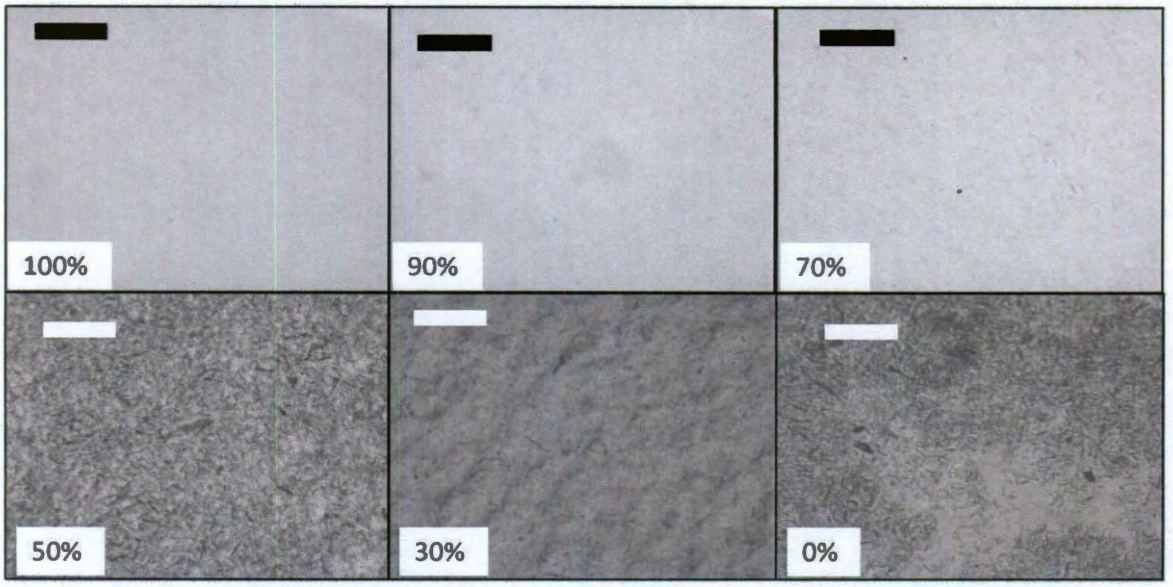

Figure 4.17: Light microscopy of SWNTs dissolved at a concentration of 3500 ppm in mixtures of 102% H_2SO_4 and $ClHSO_3$. An increasing amount of visible structure appears as the proportion of $ClHSO_3$ in the solvent is decreased because the solvent has less ability to protonate the SWNTs. Scale bars are 50 μm.

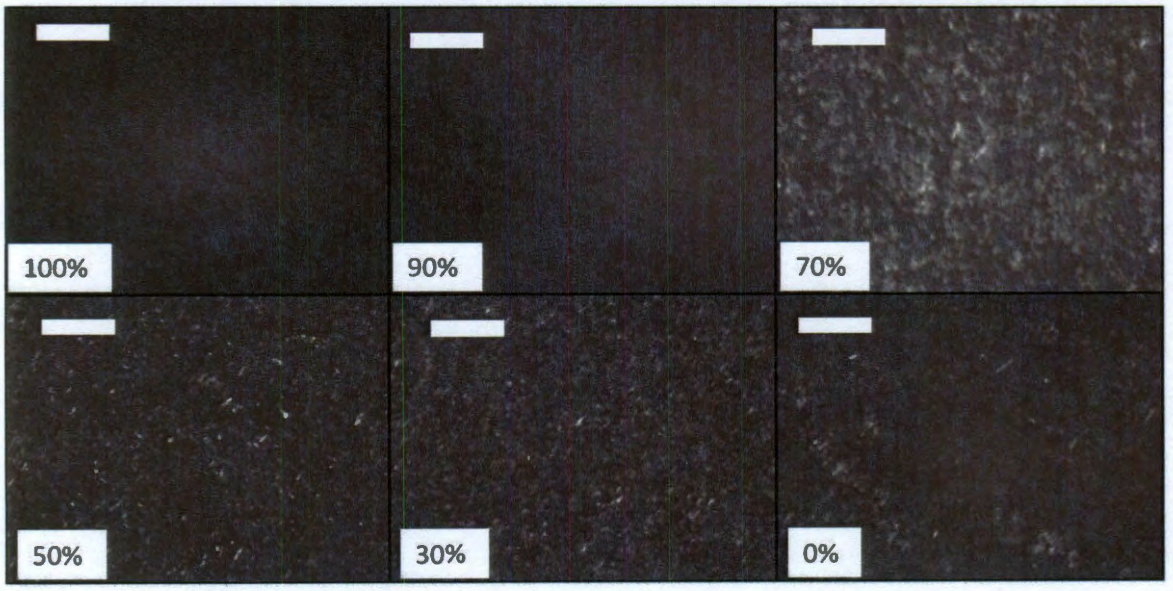

Figure 4.18: Polarized light microscopy of SWNTs dissolved at a concentration of 3500 ppm in mixtures of 102% H_2SO_4 and $ClHSO_3$. Bright domains indicate aligned SWNT liquid crystalline domains. No liquid crystal structure is visible for SWNT solutions in 100% or 90% $ClHSO_3$; Liquid crystalline structure is present in mixtures with a greater 102% H_2SO_4 content, in which the solvent has a weaker ability to protonate the SWNTs. Scale bars are 50 μm.

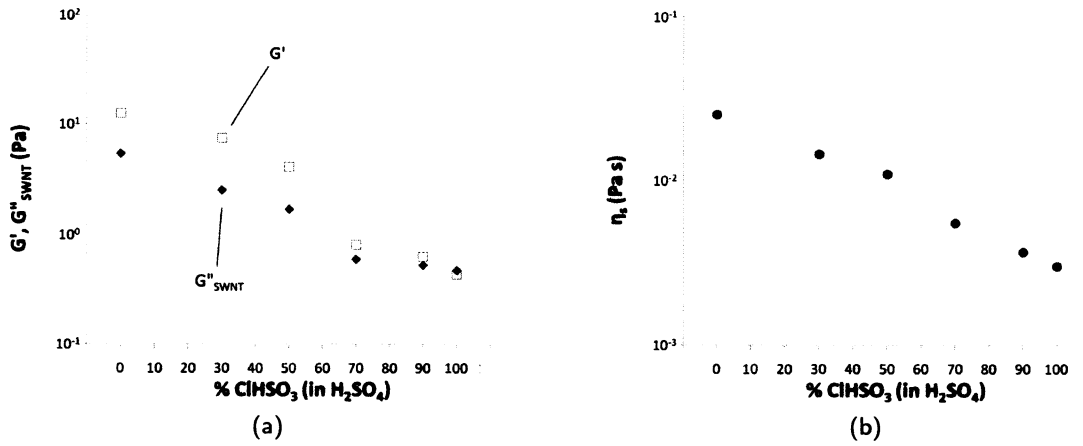

Figure 4.19: (a) G' and G''_{SWNT} vs. solvent composition for SWNTs dissolved at 3500 ppm in mixtures of $ClHSO_3$ and 102% H_2SO_4. (b) Solvent viscosity η_s of the acid mixtures used. The change in G''_{SWNT} appears to match the change in η_s, but the increase in G' is more significant and has a slightly different trend, with a greater increase between 70% and 50% $ClHSO_3$.

H_2SO_4 is added to less viscous $ClHSO_3$. Although the stress contribution of the solvent has been removed from the viscous modulus G''_{SWNT}, the viscoelastic moduli of the SWNT are still affected by the solvent viscosity through the dependence of rotational relaxation time τ_{rot} on the solvent friction factor $\zeta_\perp$. The solvent viscosity η_s for these acid mixtures is plotted in Figure 4.19 (b). A comparison between modulus and solvent viscosity shows that the increase of G''_{SWNT} does indeed parallel the increase in η_s quite closely, with both increasing by about one decade, making it plausible that solvent viscosity is largely responsible for the increase in viscous modulus.

The change in G', however, is slightly greater, and provides evidence of the change in microstructure. In particular, there is a more dramatic increase in G' between 70% and 50% $ClHSO_3$ than is observed in either G''_{SWNT} or η_s. In addition, the relative magnitude of G' with respect to G''_{SWNT} increases as the solvent becomes weaker. This ratio is plotted as a loss modulus $\tan(\delta)$ in Figure 4.20. At this concentration the loss modulus is greater than 1 only for SWNTs in 100% $ClHSO_3$, and less than 1 in all other solvents. If the SWNT viscoelasticity in these solutions were due solely to stress arising from rotational entropy, we would not expect $\tan(\delta) < 1$ at all. In the case of a SWNT network with a given elasticity and structure that are not much changed with solvent composition, we might expect an increase in $\tan(\delta)$ with the addition of H_2SO_4 due to

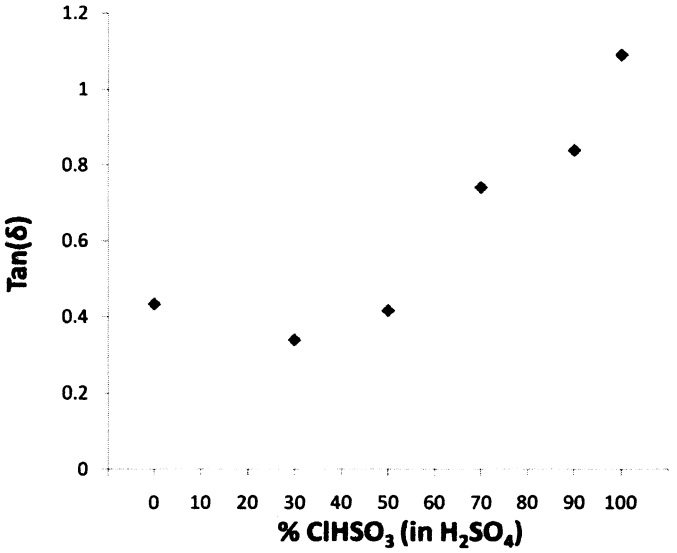

Figure 4.20: Loss modulus tan(δ) for solutions of 3500 ppm SWNT in superacids of varying strength (calculated from the data shown in Figure 4.19). The drop in tan(δ) to values lower than 1 as the proportion of 102% H_2SO_4 in the solvent increases is a strong indication that the increase in modulus values shown in Figure 4.19 reflects a change in the structure and interaction of the SWNTs, not just a change in the solvent viscosity. In solvents weaker than 50% $ClHSO_3$, a plateau occurs in tan(δ) with a value similar to the plateau observed in pure 102% H_2SO_4 above the percolation concentration.

the increase in solvent viscosity. The decrease in tan(δ) to low values that is observed instead is therefore evidence of a significant increase in SWNT structure, corroborating the observations made by light miscroscopy. Tan(δ) reaches a plateau value of ~ 0.4 in solvents having 50% or less $ClHSO_3$. This is similar to the plateau that can be observed in SWNT solutions in 102% H_2SO_4 above the percolation transition, which has a value of ~ 0.2. This, coupled with the enhanced increase in G' between 70% and 50% $ClHSO_3$, is an indication that a transition to a percolated structure at this SWNT concentration occurs between these two solvent strengths.

A second indication of the increase in structure that comes with increased SWNT attraction is the critical strain amplitude γ_c marking the limit of the linear viscoelastic regime in each of these solutions. Critical strain was determined in dynamic shear tests with a fixed frequency of 3.14 rad/s; γ_c was identified as the strain amplitude at which either G' or G''_{SWNT} deviated by more than 5% from their frequency-independent linear regime values. Figure 4.21 shown that this critical strain falls within 0.3 and 0.5 in acid mixtures comprised of 50% or more $ClHSO_3$.

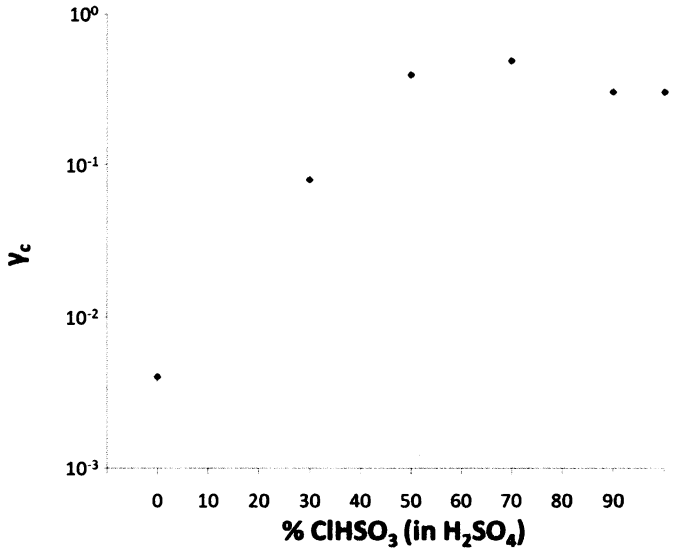

Figure 4.21: Critical strain γ_c marking the limit of the linear viscoelastic regime for SWNTs at a concentration of 3500 ppm in acid solvents of varying strength, measured in strain sweep tests at a constant frequency $\omega =$ **3.14 rad/s. The significant decrease** in γ_c in acids weaker than 50% $ClHSO_3$ is an indication of the formation of a highly inter-connected structure induced by inter-SWNT attraction.

For solvent strengths below that of 50% $ClHSO_3$, **critical strain begins to decrease significantly** with acid strength; this provides another indication that the SWNTs form an increasingly inter-connected percolated structure in solvents weaker than 50% $ClHSO_3$.

Chapter 5

Conclusion

The solvation of SWNTs in superacids such as $ClHSO_3$ and 102% H_2SO_4 is a useful technique for fluid processing applications not only because it allows for effective SWNT dispersion over a large range of concentrations but also because it provides a means of creating SWNT solutions with finely controlled attractive interactions. The fact that $ClHSO_3$ and 102% H_2SO_4 can be mixed with one another, or even diluted with water, allows researchers to create solvents with arbitrarily chosen protonating strengths. The control that can be achieved over the inter-SWNT attraction parameter using this technique makes these systems extremely interesting both from an applications standpoint and from the standpoint of theoretical study of rod systems. In this research, dynamic shear rheology and light microscopy have been used to elucidate the influence of inter-SWNT attraction on the microstructure of SWNT solutions.

Dynamic shear rheology of HiPco SWNTs in $ClHSO_3$ has been measured at concentrations ranging from the isotropic to the biphasic regime, and the results have been compared to previous measurements on HiPco SWNTs in $ClHSO_3$ at higher concentrations as well as to measurements on HiPco SWNTs in 102% H_2SO_4. The viscoelastic properties of SWNTs in superacids scale with concentration differently in different concentration regimes, reflecting the changes in SWNT microstructure due to liquid crystalline ordering and the onset of percolated network structure above a certain threshold concentration. It has been shown that the the scaling of G' and G''_{SWNT} with concentration follows roughly the same pattern in both 102% H_2SO_4 and $ClHSO_3$

as the solutions evolve from a non-percolated to a percolated structure. Comparison of the data from both acids also reveals several important differences between solutions in the two solvents, such as an increased dominance of elastic modulus at low concentrations and lower percolation threshold concentration in 102% H_2SO_4 and a lower percolation threshold concentration in 102% H_2SO_4. These differences can be ascribed to the weak attraction that exists between SWNTs in 102% H_2SO_4, which induces liquid crystalline ordering at low concentrations.

Several rheological phenomena indicate the onset of this percolated network structure in both acids: a transition to a low plateau value of γ_c, a sharp increase in elastic and viscous modulus, a sharp increase in the dominance of elastic over viscous modulus (i.e. decrease in loss modulus), and a transition to frequency-independent viscoelastic response. The transition to percolated structure occurs at higher concentration, and takes place over a more narrow concentration range, in $ClHSO_3$ than it does in 102% H_2SO_4. This is related to the differences in the onset and morphology of liquid crystalline domains in each acid. In $ClHSO_3$, percolation coincides closely with the onset of liquid crystallinity, and both transitions are driven by excluded volume interactions in a concentration isotropic SWNT network. In 102% H_2SO_4, attractive interactions cause the appearance of elongated liquid crystalline domains at concentrations far below those at which percolation is observed, and the presence of these domains in turn enables percolation at lower concentrations due to inhomogeneous arrangement of the SWNTs.

The viscoelastic properties of SWNT solutions in superacids of varying strength have also been measured. Mixing $ClHSO_3$ and 102% H_2SO_4 produces superacid solvents with a protonation strength that can be arbitrarily chosen, based on the proportions in the mixture. The protonating strength of the solvent determines the strength of attractive interactions between SWNTs in solution. If the SWNT concentration is fixed then the magnitude and relative strengths of the elastic and viscous moduli of the solution are a function of the attractive interactions, as is the degree of liquid crystalline ordering in the system. At a SWNT concentration of 3500 ppm, which falls between the percolation threshold concentrations for SWNTs in 102% H_2SO_4 and $ClHSO_3$, a transition to a more solid-like system seems to occur at a solvent strength between 50% and 70% $ClHSO_3$. This transition is indicated by a significant increase in viscoelastic moduli, a sharp

decrease in the loss modulus tan(δ) (indicating an increase in the relative strength of the elastic modulus), and the onset of a decrease in γ_c.

The results presented here can be viewed within the context of recent research that reveals the commonalies of rigid rod fluid systems across all length scales. The ability of superacids to dissolve both SWNTs and MWNTs with tunable interaction strength provides a useful model system for rod solutions. Given the availability of nanotubes from various synthesis methods, nanotubes can be obtained with a wide variety of lengths and diameters. This implies that in nanotube/superacid solutions, all four of the key properties that have been found to determine rod solution microstructure (concentration, flexibility, aspect ratio, and interaction strength) can be controlled. Future work on these systems can potentially provide insights into the behavior of a wide variety of other systems. In this research, inter-SWNT potential has been tuned from non-attractive to weakly attractive by adjusting the proportions of two superacids used in the solvent. It should also be possible to achieve even greater nanotube attraction in a controlled way through slight dilution of these superacids with water or with another miscible solvent.

The results of several recent studies have indicated that $ClHSO_3$ is a true athermal solvent for SWNTs with low defect density; this has been demonstrated through a comparison of the phase behavior with Onsager theory (Green *et al.*, 2009) and through the observation of well-dispersed individial CNTs in cryo-TEM microscopy (Parra-Vasquez *et al.*, 2010). The work presented in this thesis provides some corroboration of this finding in that percolation of SWNTs in $ClHSO_3$ is observed to manifest as an abrupt change in solution viscoelasticity such as would be expected from the formation of a glass of non-interacting rods, whereas percolation of SWNTs in 102% H_2SO_4 produces a more gradual change as concentration increases. Further confirmation has been sought by a comparison of measured SWNT viscoelasticity to a model describing isotropic,non-interacting semiflexible rods in solution, but the agreement with this model is poor for SWNTs in superacid. The resolution of this disagreement will be the subject of future study.

Because of the strong dependence of solution microstructure on inter-SWNT attractive potential, control over this attraction is an essential tool in designing SWNT solutions for applica-

tions in which there may be a need to match a desired SWNT concentration with a desired phase, degree of ordering, or viscoelastic property. Because of the moisture sensitivity and highly corrosive nature of the superacid solvents required to form true nanotube solutions, the most feasible applications for such solutions may not be those in which the fluid itself would be exploited directly, but rather those in which the acid can be removed to form a solid CNT structure or in which solvation of CNTs can be used as a means to separate different species. For these applications, the microstructure attained in the solutions remains a key parameter; it will determine how the material responds to fluid processing techniques, the mobility of individual CNTs within the solution, and the type of structures that will be present in any solid articles created using a solution as a precursor.

This study has demonstrated the effect that superacid protonating strength can have on the structure (and hence the viscoelastic properties and flow behavior) of a HiPco SWNT solution at a given concentration, as well as the effect that this parameter has in determining whether or not HiPco SWNTs form a percolated network with solid-like behavior. This knowledge can potentially be exploited in the creation of "custom" solutions of HiPco SWNTs, in which desired structure, properties, and concentration can be combined within certain limits. At this time, a thorough map has been created of the phase behavior, microstructure, and rheological properties of HiPco SWNTs over a wide range of concentrations and solvent strengths; this study forms one piece of that map. The behavior of HiPco SWNTs at low concentrations, especially in $ClHSO_3$, is still poorly explored; the application of measuring tools that avoid interference from instrument rotational inertia and have a better sensitivity to low torque measurements will be required in order to explore this regime.

The phase behavior of CNTs other than those produced by the HiPco process remains less thoroughly explored, but recent work has indicated that CNTs with a great variety of lengths and diameters can be successfully dissolved in superacids (Parra-Vasquez *et al.*, 2010). As interest in using CNTs from other sources in fluid applications arises in the future, similar techniques to those that have been employed for HiPco SWNTs can be used to determine the range of microstructures and phases achievable using those species of CNT. As has been suggested above,

CNT solutions in superacids are an example of a rod system in which each of the four essential parameters can potentially be controlled; a wide variety of solution-based CNT materials with tailored microstructures can therefore be envisioned for use in future research and applications.

Bibliography

Banzola M. *Rheology and Solubility of Solutions of Carbon-Nanotubes in Superacids.* PhD thesis (2008).

Baughman R. H., Zakhidov A. A., and de Heer W. A. (2002) Carbon nanotubes - the route toward applications. *Science* **297** [No. 5582] 787–792. Times Cited: 3196.

Bergin S. D., Nicolosi V., Streich P. V., Giordani S., Sun Z. Y., Windle A. H., Ryan P., Niraj N. P. P., Wang Z. T. T., Carpenter L., Blau W. J., Boland J. J., Hamilton J. P., and Coleman J. N. (2008) Towards solutions of single-walled carbon nanotubes in common solvents. *Advanced Materials* **20** [No. 10] 1876–+. Times Cited: 65.

Carver R. L., Peng H. Q., Sadana A. K., Nikolaev P., Arepalli S., Scott C. D., Billups W. E., Hauge R. H., and Smalley R. E. (2005) A model for nucleation and growth of single wall carbon nanotubes via the hipco process: A catalyst concentration study. *Journal of Nanoscience and Nanotechnology* **5** [No. 7] 1035–1040. Times Cited: 14.

Cicuta P., Stancik E. J., and Fuller G. G. (2003) Shearing or compressing a soft glass in 2d: Time-concentration superposition. *Physical Review Letters* **90** [No. 23]. Times Cited: 39.

Dai H. J. *Nanotube Growth and Characterization* pages 29–54. Springer New York (2001).

Davis V. A. *Phase Behavior and Rheology of Single-Walled Carbon Nanotubes (SWNTs) in Superacids with Application to Fiber Spinning.* PhD thesis (2006).

Davis V. A., Ericson L. M., Parra-Vasquez A. N. G., Fan H., Wang Y. H., Prieto V., Longoria J. A., Ramesh S., Saini R. K., Kittrell C., Billups W. E., Adams W. W., Hauge R. H., Smalley R. E., and Pasquali M. (2004) Phase behavior and rheology of swnts in superacids. *Macromolecules* **37** [No. 1] 154–160. Times Cited: 128.

Davis V. A., Parra-Vasquez A. N. G., Green M. J., Rai P. K., Behabtu N., Prieto V., Booker R. D., Schmidt J., Kesselman E., Zhou W., Fan H., Adams W. W., Hauge R. H., Fischer J. E., Cohen Y., Talmon Y., Smalley R. E., and Pasquali M. (2009) True solutions of single-walled carbon nanotubes for assembly into macroscopic materials. *Nature Nanotechnology* **4** [No. 12] 830–834. Times Cited: 11.

Doi M. and Edwards S. F. (1978) Dynamics of rod-like macromolecules in concentrated-solution .1. *Journal of the Chemical Society-Faraday Transactions Ii* **74** 560–570. Times Cited: 391 3.

Doi M. and Edwards S. F. *The Theory of Polymer Dynamics.* International Series of Monographs on Physics. Oxford Science Publications Oxford (1986).

Donald A. M. and Windle A. H. *Liquid Crystal Polymers.* Cambridge University Press Cambridge (1992).

Dresselhaus M. S. and Avouris P. *Introduction to Carbon Materials Research* pages 1–9. Springer New York (2001).

Duque J. G., Parra-Vasquez A. N. G., Behabtu N., Green M. J., Higginbotham A. L., Price B. K., Leonard A. D., Schmidt H. K., Lounis B., Tour J. M., Doorn S. K., Cognet L., and Pasquali M. (2010) Diameter-dependent solubility of single-walled carbon nanotubes. *Acs Nano* **4** [No. 6] 3063–3072. Times Cited: 5.

Ebbesen T. W., Lezec H. J., Hiura H., Bennett J. W., Ghaemi H. F., and Thio T. (1996) Electrical conductivity of individual carbon nanotubes. *Nature* **382** [No. 6586] 54–56. 10.1038/382054a0.

Ericson L. M., Fan H., Peng H. Q., Davis V. A., Zhou W., Sulpizio J., Wang Y. H., Booker R., Vavro J., Guthy C., Parra-Vasquez A. N. G., Kim M. J., Ramesh S., Saini R. K., Kittrell C., Lavin G., Schmidt H., Adams W. W., Billups W. E., Pasquali M., Hwang W. F., Hauge R. H., Fischer J. E., and Smalley R. E. (2004) Macroscopic, neat, single-walled carbon nanotube fibers. *Science* **305** [No. 5689] 1447–1450. Times Cited: 193.

Fakhri N., Tsyboulski D. A., Cognet L., Weisman R. B., and Pasquali M. (2009) Diameter-dependent bending dynamics of single-walled carbon nanotubes in liquids. *Proceedings of the National Academy of Sciences of the United States of America* **106** [No. 34] 14219–14223. Times Cited: 13.

Fakhri N., MacKintosh F. C., Lounis B., Cognet L., and Pasquali M. (2010) Brownian motion of stiff filaments in a crowded environment. *Science* **330** [No. 6012] 1804–1807. Times Cited: 2.

Flory P. J. (1956) Phase equilibria in solutions of rod-like particles. *Proceedings of the Royal Society of London Series a-Mathematical and Physical Sciences* **234** [No. 1196] 73–89. Times Cited: 1163.

Gabriel J. C. P. and Davidson P. (2003) Mineral liquid crystals from self-assembly of anisotropic nanosystems. *Colloid Chemistry 1* **226** 119–172. Times Cited: 0 Antonietti, M Antonietti, M.

Gao G. H., Cagin T., and Goddard W. A. (1998) Energetics, structure, mechanical and vibrational properties of single-walled carbon nanotubes. *Nanotechnology* **9** [No. 3] 184–191. Times Cited: 184 5th Foresight Conference on Molecular Nanotechnology NOV 05-08, 1997 PALO ALTO, CALIFORNIA.

Green M. J., Parra-Vasquez A. N. G., Behabtu N., and Pasquali M. (2009) Modeling the phase behavior of polydisperse rigid rods with attractive interactions with applications to single-walled carbon nanotubes in superacids. *Journal of Chemical Physics* **131** [No. 8]. Times Cited: 6.

Hamada N., Sawada S., and Oshiyama A. (1992) New one-dimensional conductors - graphitic microtubules. *Physical Review Letters* **68** [No. 10] 1579–1581. Times Cited: 2239.

Hobbie E. K. and Fry D. J. (2007) Rheology of concentrated carbon nanotube suspensions. *Journal of Chemical Physics* **126** [No. 12]. Times Cited: 37.

Hone J., Whitney M., Piskoti C., and Zettl A. (1999) Thermal conductivity of single-walled carbon nanotubes. *Physical Review B* **59** [No. 4] R2514–R2516. Times Cited: 160.

Hone J., Llaguno M. C., Nemes N. M., Johnson A. T., Fischer J. E., Walters D. A., Casavant M. J., Schmidt J., and Smalley R. E. (2000) Electrical and thermal transport properties of magnetically aligned single walt carbon nanotube films. *Applied Physics Letters* **77** [No. 5] 666–668. Times Cited: 278.

Hough L. A., Islam M. F., Janmey P. A., and Yodh A. G. (2004) Viscoelasticity of single wall carbon nanotube suspensions. *Physical Review Letters* **93** [No. 16]. Times Cited: 54.

Hudson J. L., Casavant M. J., and Tour J. M. (2004) Water-soluble, exfoliated, nonroping single-wall carbon nanotubes. *Journal of the American Chemical Society* **126** [No. 36] 11158–11159. Times Cited: 122.

Kayatin M. J. *Rheology, structure, and stability of carbon nanotube - unsaturated polyester resin dispersions (Master's Thesis).* PhD thesis (2008).

Kirkwood J. G. and Plock R. J. (1956) Non-newtonian viscoelastic properties of rod-like macromolecules in solution. *Journal of Chemical Physics* **24** [No. 4] 665–669. Times Cited: 56.

Krishnan A., Dujardin E., Ebbesen T. W., Yianilos P. N., and Treacy M. M. J. (1998) Young's modulus of single-walled nanotubes. *Physical Review B* **58** [No. 20] 14013–14019. Times Cited: 616.

Larson R. G. *The Structure and Rheology of Complex Fluids.* Oxford University Press Oxford (1999).

Ma A. W. K., Nam J., Behabtu N., Young C., Dan B., Tsentalovich D., Majumder M., Song L., Cohen Y., Ajayan P. M., and Pasquali M. (2011) Scalable formation of carbon nanotube films containing highly aligned whisker-like crystallites by dip coating and solvent extraction. In preparation.

Macosko C. *Rheology: Principles, Measurements, and Applications.* Advances in Interfacial Engineering. Wiley-VCH New York (1994).

Marrucci M. and Gizzuti N. (1983) Predicted effect of polydispersity on rodlike polymer behavior in concentrated solutions. *Journal of Non-Newtonian Fluid Mechanics* **14** 103–119.

Mezger T. *The rheology handbook: for users of rotational and oscillatory rheometers.* Coatings Compendien. Vincentz Network (2006). ISBN 9783878701743. URL `http://books.google.com/books?id=N9FdnOMEIDIC`.

Morse D. C. (1998) Viscoelasticity of concentrated isotropic solutions of semiflexible polymers. 2. linear response. *Macromolecules* **31** [No. 20] 7044–7067. Times Cited: 128.

Morse D. C. (1999) Viscoelasticity of concentrated isotropic solutions of semiflexible polymers. 3. nonlinear rheology. *Macromolecules* **32** [No. 18] 5934–5943. Times Cited: 11.

Odijk T. (1983) On the statistics and dynamics of confined or entangled stiff polymers. *Macromolecules* **16** [No. 8] 1340–1344. Times Cited: 238.

Parra-Vasquez A. N. G. *Solubility, Length Characterization, and Cryo-TEM of Pristine and Functionalized Single-Walled Carbon Nanotubes in Surfactant and Superacid Systems, With Application to Spinning SWNT Fibers.* PhD thesis (2009).

Parra-Vasquez A. N. G., Behabtu N., Green M. J., Pint C. L., Young C. C., Schmidt J., Kesselman E., Goyal A., Ajayan P. M., Cohen Y., Talmon Y., Hauge R. H., and Pasquali M. (2010) Spontaneous dissolution of ultralong single- and multiwalled carbon nanotubes. *Acs Nano* **4** [No. 7] 3969–3978. Times Cited: 0.

Penicaud A., Poulin P., Derre A., Anglaret E., and Petit P. (2005) Spontaneous dissolution of a single-wall carbon nanotube salt. *Journal of the American Chemical Society* **127** [No. 1] 8–9. Times Cited: 93.

Ramesh S., Ericson L. M., Davis V. A., Saini R. K., Kittrell C., Pasquali M., Billups W. E., Adams W. W., Hauge R. H., and Smalley R. E. (2004) Dissolution of pristine single walled carbon nanotubes in superacids by direct protonation. *Journal of Physical Chemistry B* **108** [No. 26] 8794–8798. Times Cited: 78.

Shetty A. M., Spicer P., and Solomon M. J. Direct visualization of glassy dynamics in a model polyamide rod system (2010).

Solomon M. J. and Spicer P. T. (2010) Microstructural regimes of colloidal rod suspensions, gels, and glasses. *Soft Matter* **6** [No. 7] 1391–1400. Times Cited: 3.

Teraoka I. and Hayakawa R. (1989) Theory of dynamics of entangled rod-like polymers by use of **a mean-field green-function formulation .2. rotational diffusion.** *Journal of Chemical Physics* **91** [No. 4] 2643–2648. Times Cited: 31.

Thess A., Lee R., Nikolaev P., Dai H. J., Petit P., Robert J., Xu C. H., Lee Y. H., Kim S. G., Rinzler A. G., Colbert D. T., Scuseria G. E., Tomanek D., Fischer J. E., and Smalley R. E. (1996) Crystalline ropes of metallic carbon nanotubes. *Science* **273** [No. 5274] 483–487. Times Cited: 3299.

Trappe V. and Weitz D. A. (2000) Scaling of the viscoelasticity of weakly attractive particles. *Physical Review Letters* **85** [No. 2] 449–452. Times Cited: 120.

Vigolo B., Penicaud A., Coulon C., Sauder C., Pailler R., Journet C., Bernier P., and Poulin P. (2000) Macroscopic fibers and ribbons of oriented carbon nanotubes. *Science* **290** [No. 5495] 1331–1334. Times Cited: 723.

Walters D. A., Ericson L. M., Casavant M. J., Liu J., Colbert D. T., Smith K. A., and Smalley R. E. (1999) Elastic strain of freely suspended single-wall carbon nanotube ropes. *Applied Physics Letters* **74** [No. 25] 3803–3805. Times Cited: 305.

Wei B. Q., Vajtai R., and Ajayan P. M. (2001) Reliability and current carrying capacity of carbon nanotubes. *Applied Physics Letters* **79** [No. 8] 1172–1174. Times Cited: 327.

Xu Y. Q., Peng H. Q., Hauge R. H., and Smalley R. E. (2005) Controlled multistep purification of single-walled carbon nanotubes. *Nano Letters* **5** [No. 1] 163–168. Times Cited: 62.

Yamamoto T., Watanabe K., and Hernandez E. R. (2008) Mechanical properties, thermal stability and heat transport in carbon nanotubes. *Carbon Nanotubes* **111** 165–194. Times Cited: 1.

Yu M. F., Files B. S., Arepalli S., and Ruoff R. S. (2000) Tensile loading of ropes of single wall carbon nanotubes and their mechanical properties. *Physical Review Letters* **84** [No. 24] 5552–5555. Times Cited: 850.